NATIONAL UNIVERSITY of SCIENCE and TECHNOLOGY POLITEHNICA BUCHAREST

Doctoral School of Engineering and Applications of Lasers and Accelerators

Doctoral Thesis

Summary

Towards laser-based interferometric breast radiography

Supervisors: Prof. Dr. Calin Alexandru Ur

Dr. Dan Stutman

Author: Safca Ștefania-Nicoleta

Bucharest 2024

Acknowledgments

I want to express my appreciation to those who have played a significant role and contributed to completing the scientific work for my doctoral thesis.

To begin with, I want to express my gratitude to my academic advisor, Professor Dr. Calin Alexandru Ur, for accepting me into his doctoral program and for providing me the chance to engage in such an important research project with significant medical and physical relevance, but also with a possible future substantial societal impact.

I thank my coordinator, Dr. Dan Stutman, who guided, supported, and mentored me scientifically throughout my entire research journey and in the elaboration of my doctoral thesis. His expertise, valuable insights, and constructive feedback have been instrumental in shaping this thesis and my future in research. I am grateful for all the patience and challenging discussions, for teaching me and revealing the subtleties of the phase contrast imaging technique, which cannot be learned by reading but by passing on, and for the endless disapproval that made me work harder and wish to improve.

I also wish to convey my appreciation to Dr. Florin Negoita for the trust offered from my beginnings at ELI-NP and for all the support, help, and guidance in building and commissioning the X-ray Imaging Laboratory, which has been instrumental for the research work presented in this thesis. I am also thankful for initiating me in the FLUKA code and for all his support in developing a procedure for calculating the absorbed dose for the specific case of breast interferometric radiography, which is extremely valuable and essential for the research showcased in this work.

I am grateful to all my thesis advising committee members, Dr. Calin Alexandru Ur, Dr. Dan Stutman, Dr. Florin Negoita, and Dr. Ion Tiseanu, for their time, knowledge, and critical evaluation during exams and scientific activity reports. Their feedback and recommendations have enriched the quality of my research for this thesis.

I particularly thank Dr. Bogdan Tanase and Dr. Mihai Ceausu from the Oncological Institute “Professor Doctor Alexandru Trestioreanu” from Bucharest for providing samples of different types of breast cancer embedded in paraffin and for the histopathological analysis of the samples.

In the same measure, I want to thank Dr. Mihai Radu and Dr. Cosmin Mustaciosu for providing animal tissue from a rat for different tests and optimizations of the developed interferometer.

Big thanks to my team from X-ray Imaging Laboratory, who has been by my side throughout this engaging and sometimes stressful period, made me laugh, shared their experience, and supported me emotionally and professionally.

The research presented in this work received support from the ELI-NP project—Phase I and Phase II, co-financed by the Romanian Government and the European Union through the European Regional Development Fund: the Competitiveness Operational Program (1/07.07.2016, C.O.P., ID 1334). Additionally, support was extended through the Impulse project (Integrated Management and Reliable Operations for User-based Laser Scientific Excellence) under the H2020 initiative, with project number 871161.

Table of Contents

Introduction

X-ray imaging stands as a highly valuable diagnostic tool in medicine, science, and industry. Following the groundbreaking discovery of W. C. Rontgen of X-rays in 1895, their remarkable ability to penetrate matter and enable "visualizing the interior of objects and the human body" has led to extensive utilization, research, and enhancement of X-ray imaging techniques across various fields, meeting diverse requirements and evolving with the times. The entire traditional X-ray imaging medicine diagnostic relies on the absorption process, more precisely on the difference of absorption in distinct layers, structures, and thicknesses of tissues, bones, and organs. The big problem with this technique is that almost all soft tissues from the human body, composed of low Z elements, are nearly invisible to the X-rays necessary to penetrate the body, and poor contrast images are obtained. The poor visibility of soft tissues in hard X-rays and low atomic number materials became evident as quantum physics advanced [1, 2]. According to the particle description of light, until the threshold for pair production at 1.02 MeV is reached, X-rays primarily interact with matter through two main mechanisms: the photoelectric effect and inelastic or incoherent (Compton) scattering. These two mechanisms are completed by the elastic or coherent (Rayleigh) scattering, which corresponds to wave formalism. Among these three mechanisms, the photoelectric effect is the main responsible for creating X-ray images by absorbing photons [3]. The linear photoelectric absorption coefficient (μ_{ph}) rapidly decreases to minimal values as the X-ray energy (E) increases and the atomic number of the material decreases. The typical medical diagnostic energy dependence is approximately $\mu_{ph} \propto Z^4/E^3$. For example, at 60 keV, μ_{ph} is approximately 0.014 cm^{-1} for muscle tissue, meaning that a layer around 1.5 cm thick is necessary to absorb 2% of the X-ray beam. Furthermore, X-ray absorption does not differentiate well between low Z materials. As an example, the disparity in X-ray absorption between muscle and adipose tissue at 60 keV is only approximately $\Delta\mu_{ph} = 0.007$ cm^{-1} [4].

A first solution to this problem is to decrease the X-ray energy below a few tens of keV, where absorption becomes significant and soft tissues can be imaged. However, this low energy does not allow imaging of objects thicker than a few centimeters and increases the radiation dose to the patient since just a few percent of the incident radiation is transmitted and used to produce the radiography. Another way to solve the poor visibility between different types of tissue, like muscle, fat, tumor, or abnormalities, is using more images from different viewing angles

(tomosynthesis or tomography). In this case, the differentiation between soft tissues is improved, but the dose to the patient is increased, and frequent investigations are not recommended.

Because of the above presented shortcomings, over the past three decades, a new technique of imaging based on refraction instead of absorption has been intensively investigated for medical applications - Phase Contrast Imaging [5, 6, 7, 8]. The attention received by this technique is first because the refraction mechanism in the materials with low Z is at least three orders of magnitude stronger than the attenuation one, enabling a high sensitivity for the identification of much smaller density variations in soft tissues. Second, the coefficient of phase change of the X-ray wave per unit length ($\varphi = 2\pi\delta/\lambda$, with δ the real part of the refractive index) decreases slower with the energy than the coefficient of attenuation ($\mu = 4\pi\beta/\lambda$, with β the imaginary part of the refractive index), ($1/E$ versus $1/E^3$), allowing in this way to reduce the radiation dose delivered to patient by using higher energies where the investigated tissue is less absorbing [4, 6]. Lastly, δ is directly linked to the electron density in matter, which enables quantitative phase contrast imaging. Nevertheless, while phase offers a much better image contrast mechanism than absorption, measuring phase shifts for diagnostic X-rays is not trivial. Different phase-sensitive methods and configurations were developed, exploiting the mechanisms of diffraction and interference to convert the phase shift into detectable changes in intensity, as the refraction angles in soft tissues are of the order of μradians and cannot be solved directly by state-of-the-art detectors [7].

The X-ray phase measurement methods are classified into genuine two-beam interferometry (TBI) and refraction-based methods. TBI has a high sensitivity to the absolute phase change of the X-rays but requires monochromatic crystal optics and synchrotron X-ray sources, which limits its clinical applicability [9, 10]. On the other hand, refraction-based methods are more versatile, suitable for clinical implementation, and can be further classified as follows:

- Propagation phase contrast imaging (PBI): This approach does not involve optics and relies on the measurement of the spatial coherence of the incident wave. PBI is a widely used and straightforward technique which exhibits sensitivity to the second derivative of the phase shift. However, its sensitivity is limited as significant values of the second derivative of the phase shift are mainly present near the edges of the object [11].
- Methods with X-ray optics: These techniques are sensitive to the first derivative of the phase shift, corresponding to the distribution of the refraction angle. Among these methods, the microgrid or mask methods are commonly employed in research for medical applications. They can operate with broad X-ray spectra and large spot sizes of medical X-ray tubes. The underlying concept of these methods is to structure the X-ray beam that illuminates the object to create an intensity micropattern at the detector, such as a system of parallel fringes. If a refractive object is placed into the beam, the pattern shifts proportionally to the refraction angle. An absorption grid is then positioned at the detector to transform the pattern changes into intensity modulations [12].

Several methods for phase-contrast imaging based on refraction have been developed, utilizing interference and diffraction to convert phase changes into measurable intensity variations. Among them, the most important are propagation-based imaging, analyzer-based imaging, grating interferometry, edge illumination, and speckle-based phase contrast imaging [5, 6, 13, 14, 15, 16]. The grating interferometry and edge illumination techniques received special attention due to a critical advantage: these techniques are compatible with wide X-ray spectra and extended X-ray sources, including high-power medical X-ray tubes [7, 16, 17, 18, 19]. These refraction-based methods offer alternative approaches to capture and measure the phase information of X-rays, providing enhanced imaging capabilities for medical applications and may bring real improvements and additional information in medical diagnostic imaging due to its much higher sensitivity to soft tissue density variations than absorption-based X-ray imaging. Over the years, this fact attracted the interest of many researchers.

Because of the versatility offered by the grating interferometry technique, it has been intensely investigated for medical applications [5, 7, 19]. Recently, dark-field X-ray radiography has been successfully evaluated on patients for diagnosis of lung pathologies such as emphysema and COPD [20, 21], and dark-field computed tomography (CT) of the lung has begun translation into the clinic [22]. Nevertheless, there are still some significant challenges to reaching the full potential of grating-based PXI for clinical implementation, particularly regarding refraction-based imaging. Among the most important, we mention limited sensitivity to small tissue density differentials due to limited angular sensitivity, high radiation dose, and long scan time. All these challenges are interconnected.

In this thesis, the problem of mammography is addressed and a possible additional method for the early identification of breast cancer with higher sensitivity and a low dose is investigated and developed. Other potential applications of phase-contrast imaging in medicine are explored. Breast cancer ranks as the second most common cause of death among women under the age of 50, following lung cancer. It remains a substantial contributor to mortality even beyond this age group. The key to reducing mortality is the early detection of breast tumors. X-ray radiography of the breast (mammography), based on the absorption of low-energy X-rays in soft tissues, is the "gold standard" investigation used for large-scale screening of the female population against breast cancer [23, 24]. Mammography aims to detect sub-millimeter and millimeter size soft tissue tumoral masses, slightly denser than normal tissue, constituting an early sign of cancer. Microcalcifications with a few hundred micrometers in size are also considered potential signs of malignity [25].

Current mammography, which relies on X-ray absorption, has two significant shortcomings. The first is insufficient sensitivity and specificity to early-stage cancers due to poor differentiation between tumor and normal tissues. The reason is that the difference in X-ray absorption between normal and tumor soft tissue is minimal. This leads to missed early-stage cancers and a substantial fraction of false-positive diagnostics [24, 26]. The second shortcoming is the relatively large radiation dose delivered to the breast. To obtain image contrast for soft

tissues, the typical mean X-ray energy used in mammography is below 20 keV, where the breast becomes highly absorbing. At this energy, over 90% of the incoming X-rays are absorbed by the breast, and only the remaining 10% are used to produce the mammogram. This leads to a large radiation dose delivered to the breast of up to 3- 5 mGy in a conventional mammogram. Frequent mammography (more than once every two years) for detecting and monitoring early-stage cancers or breast cancer screening is not recommended. More than that, because of the breast structure and high tissue density, in young women, under 40, the mammogram is not indicated because of the high absorption in the mammary tissue that leads to high radiation dose and increased incidence of false-positive or false-negative results [26].

Even though the grating-based imaging methods can work with a conventional X-ray tube, as the work presented in this thesis and literature shows, there is room to improve the technique considerably and achieve the maximum potential of phase contrast imaging for medical applications. Conventional X-ray sources are not ideal for ultrahigh sensitivity interferometric mammography from the point of view of exposure time, sensitivity, spatial resolution, and fringe visibility. They emit radiation isotropically in all directions and do not provide enough photons for fast clinical imaging at large distances. The ideal source for interferometric mammography should emit a photon fluence of the order of 10^{10} photons/ mm^2 or more over an area covering the compressed breast at a distance of up to several meters. Ideally, the source spot size should be in the 1 µm range (spatially coherent), which will strongly improve spatial resolution, enhance the phase effects, and eventually eliminate the need for source grating. X-ray sources powered by high-intensity lasers could be ideally suited for this type of medical application. They are significantly brighter and more focused than conventional X-ray tubes, emitting a substantial quantity of photons over extended distances in a narrow cone and within extremely short timeframes.

Considering all these aspects, the combination between high-intensity laser-based X-ray sources and long Talbot-Lau interferometers may provide a new or alternative tool for high-sensitivity and low-dose mammography.

This work is structured as follows:

Chapter 1 and *Chapter 2* provide a comprehensive overview of the theoretical background that forms the foundation of the thesis, with a specific focus on justifying the theoretical considerations within the context of using the phase contrast imaging technique for breast radiography. A short description of the current phase-sensitive methods and the theoretical fundaments for grating-based imaging using X-ray Talbot-Lau interferometry is outlined together with a concise summary of the morphology and the pathology of the breast. The disadvantages of conventional mammography are presented with the limitation of the technique, and the advantages offered by phase contrast imaging for breast radiography are highlighted. The entire construction of these chapters emphasizes and evidentiates the fundamental elements for understanding the

importance and the need for long interferometers with ultrahigh visibility, high fringe visibility, and a novel X-ray source generated with high-power lasers suitable for medical applications.

Chapter 3 presents the results of ultrahigh sensitive phase-contrast imaging experiments conducted at the XIL laboratory and the Department of Physics and Astronomy at Johns Hopkins University in Baltimore, USA, outlining the collaborative effort between ELI-NP and the JHU. Three main setups are presented: ultrahigh sensitivity interferometer for breast radiography, glancing ultrahigh angle interferometer for breast radiography, and high sensitivity interferometer for artery radiography. In the first part of this chapter, a detailed depiction of the assembly and optimization of the Talbot-Lau interferometer designed explicitly for breast imaging is done. Additionally, potential approaches for implementing this technique in cardio-pulmonary applications are explored. Results obtained at a record angular sensitivity of 0.82 μradians on objects mimicking tumoral structures from an accredited mammography phantom, an actual tumor breast embedded in paraffin, a human artery immersed in water, and a rat heart immersed in water and air are presented.

The *final Chapter* proposes integrating ultrahigh sensitive long interferometers with bright, intense, well-focused, and spatially coherent laser-based X-ray sources. Such a combination has the potential to yield substantial advantages in multiple aspects. Potential advantages and requirements of the X-ray sources generated with high-power lasers for medical interferometry, perspectives, and practical considerations for laser-based medical interferometric imaging are presented.

In C*onclusion*, the scientific results are summarized, and future perspectives are discussed

Chapter 1: Theoretical Background

This chapter provides an accurate image of the theoretical background that is the basis of the thesis, with a particular emphasis on explaining and justifying theoretical aspects of the physics behind breast radiography. It begins by describing the existing X-ray sources and the interaction of X-rays with matter. These descriptions and interpretations were deduced from the work of Als-Nielsen and McMorrow (Elements of Modern X-ray Physics, 2011) [1], A.G. Michette, C.J. Buckley (X-Ray Science and Technology, 1993) [2] and Knoll Glen (Radiation Detection and Measurement, 2010) [3]. The nature of X-rays and all the properties illustrated in this chapter suggest why Phase Contrast X-ray imaging methods have the capability to outperform the results of conventional absorption-based techniques in soft tissue evaluation and become an additional method for breast screening and not only.

Furthermore, the chapter provides a concise overview of the currently established X-ray phase-sensitive techniques and introduces the theoretical aspects of X-ray imaging using Talbot-Lau interferometry. Finally, the chapter concludes by providing a concise summary of the structure and pathological alterations in the female breast, along with the clinical methods for diagnosis, treatment alternatives for breast conditions, and a brief discussion on dose considerations.

1.1. History and Overview of X-ray Sources

Following the discovery of Wilhelm Conrad Röntgen in 1895 of X-rays and their utilization in imaging, a design for X-ray tube sources was developed and subsequently employed in hospitals and laboratories. The operating principle of X-ray tubes is based on the acceleration at high voltages, typically several tens of kilovolts, of the electrons emitted by a cathode towards an anode with a high atomic number.

Remarkable progress in enhancing the characteristics of X-rays became evident through the development of synchrotron sources. These sources initially utilized radiation emitted as a parasite from particle accelerators (1st generation), and afterward, dedicated facilities were explicitly constructed for X-ray experiments (2nd). Synchrotron sources entail the acceleration of electrons to relativistic energies, followed by their circulation within a storage ring. A circular trajectory is induced for these electrons through the application of bending magnets. As these electrons undergo acceleration, they emit a broad radiation spectrum within a narrow cone. Synchrotron sources exhibit a significantly higher brilliance, superior to X-ray tubes by several orders of magnitude. This improvement is achieved through two factors: an increased photon flux and a substantially reduced solid angle from which the radiation is emitted. In recent developments, 3rd generation synchrotron sources have further elevated the brilliance by implementing smaller electron beams, resulting in a smaller spot size.

Synchrotrons are primarily utilized in biology, particularly in proteomics and fundamental physics experiments. They stand out as the leading non-bremsstrahlung sources of X-radiation and have also been applied in various medical imaging research, including propagation-based phase-contrast imaging in mammography [27, 28, 29].

1.2. X-rays fundamentals

X-ray radiation is a type of electromagnetic radiation distinguished by wavelengths spanning from 0.01 to 10 nm. X-rays can be classified as "hard" or "soft" based on their energy, with the threshold typically set at 5-10 keV [2]. In medical imaging, X-rays with high energies are employed to ensure penetration. When X-rays interact with tissue, specifically the atoms within it, they can experience various types of interactions. The incoming X-ray photon can be scattered or photoelectrically absorbed. Scattering can be an elastic process, where the wavelength of the photon remains unchanged, or an inelastic process, where the wavelength is altered. While many studies focus on the particle-like properties of X-rays, it is also essential to consider the wave nature of X-rays when analyzing their interaction with matter. In the wave formalism, the interaction between X-rays and matter can be depicted through the complex index of refraction, which takes into account both the real (representing refraction) and imaginary (representing absorption) components of the properties of the material. Wave formalism provides a comprehensive framework for understanding and analyzing X-rays interactions with condensed matter. The definition of the complex index of refraction is as follows:

$$n = 1 - \delta + i\beta \tag{1.1}$$

Here, δ represents the refractive index decrement, providing the phase shift of the wave, and β corresponds to the absorption index.

1.3. Phase Contrast Imaging Techniques

While variations in intensity caused by attenuation are directly detected utilizing a detector, measuring phase change requires an indirect approach. Various methods can be employed to convert phase changes of the incident X-ray wave into measurable intensity changes. Detailed reviews on this topic can be found in References [30, 31, 32, 33, 34]. Here, an overview of their main characteristics is provided, focusing on evaluating their sensitivity in the context of implementing them in practical clinical uses with X-ray sources based on lasers. As mentioned in the introduction, there are two main classes of approaches: genuine two-beam interferometry, sensitive to the absolute phase change in the thickness of the material, regardless of the density gradient, and refraction-based methods for measuring the differential phase change on refraction index gradients.

Two-beam interferometry, also known as Cristal Interferometry, is the oldest and most sensitive phase-based imaging technique pioneered by Bonse and Hart in 1965 and employed X-ray beam-splitters and reflectors made from a single silicon crystal block to implement this technique [35]. Crystal interferometry for phase contrast imaging typically involves using four silicon beam splitters arranged in a Laue configuration. These splitters generate two individual beams, with the sample placed in one of them. The other three beam splitters are necessary for recombining and enabling interference between the two beams. After the recombination of the two beams, a microscopic fringe pattern is formed through interference. From this fringe pattern, the absolute phase change introduced by the object is calculated [36].

Propagation-based imaging (PBI) is the least complex approach for phase-contrast imaging and does not require additional X-ray optics [37, 38]. This technique takes advantage of the strong refraction that happens at the edges of the sample, where the refraction angles can reach tens of microradians. The refraction is proportional to the gradient of the areal electron density, making the edges of the sample the region with the highest refraction. In PBI, the analyzed object must be illuminated with a small spot X-ray source, typically within the micron scale, and the distance after the X-ray passes through the object (distance between the sample and the detector) should be on the scale of meters. This propagation distance enables the X-rays refracted at the object edges to interfere, resulting in intensity modulations at the boundaries of the sample. A small X-ray spot with spatial quasi-coherence is necessary to ensure that the narrow fringes remain distinct on the X-ray detector. PBI works well with spectrally broad X-ray sources, such as conventional tubes, due to the relatively slow variation of the X-ray refraction coefficient with

energy [39]. PBI is often preferred in practical applications because of its simplicity, ease of implementation, and broad spectral bandwidth. It has been successfully used with laser-based X-ray sources as well [40].

Grating-based Interferometry (GBI) interferometry is illustrative for deflectometry family methods, and it is considered one of the most suitable approaches for clinical implementation in phase contrast imaging. A detailed and comprehensive description of this technique can be found in Chapter 2.

1.4.The female breast

Among women, mammary cancer is the most aggressive form of cancer and ranks as the second most common cause of cancer-related deaths, following lung cancer. In 2020, breast malignancy was diagnosed in 2.3 million women worldwide, and there were 685,000 reported deaths due to the disease. These statistics underscore the substantial worldwide impact of this disease. Since 2021, breast cancer has taken the lead as the most frequently diagnosed cancer, overtaking lung cancer. In Romania, breast cancer has the highest incidence among neoplasms affecting women, and mortality rates are above the EU average. If current trends remain unchanged, the World Health Organization (WHO) predicts that by 2040, more than 3 million new cases and 1 million deaths will be because of population growth and aging. These statistics highlight the urgent necessity for continued research efforts, advancements in early detection techniques, and improvements in treatment modalities for women affected by breast cancer [23].

Chapter 2: Ultrahigh Sensitivity Grating-based Interferometry

This chapter provides an overview of grating interferometry and the advantages brought by this technique. It begins by introducing the operational principle and the main characteristics that determine the huge potential and benefits of the method. The chapter then continues with a more detailed discussion of the physical effects involved, such as the Talbot effect, the need for ultrahigh sensitivity, and different types of grating-based interferometers. An essential part of this chapter is to outline the core elements required for understanding the necessity of long interferometers, ultrahigh visibility, and good fringe visibility.

In the end, the chapter focuses on the analytical methods used to retrieve information regarding the phase variation from the acquired data. Phase-stepping, Moiré fringes, and refraction-enhanced technique are discussed in detail, as they allow for straightforward data processing and provides high spatial resolution and additional information.

2.1. Working principle - Talbot-Lau Interferometer

The grating-based interferometry relies on the Talbot-Lau interferometer, which utilizes three gratings with micron-size periods: two absorption gratings (G0 and G2) and a transmission grating (G_1). These gratings are positioned at approximately 1-meter intervals to create a large-area angular collimator. This collimator converts the tiny X-ray angular displacement caused by refraction into intensity changes on a conventional detector. The fundamental principle behind this method is the Talbot effect, which involves the formation of a fringe pattern with the same period as the transmission (phase) grating (G_1) at specific intervals along the beam, known as Talbot distances. The fringe pattern becomes distorted or shifted when a refractive sample is inserted into the beam. The shifts in the fringe pattern are then converted into changes in intensity by using an absorption grating (G_2) with a period corresponding to the one of the Talbot pattern. Furthermore, to enable the method to function with an extended X-ray source spot, an absorption grating (G_0) is placed next to the source to divide it into smaller spatially coherent emitters. [16, 17, 18].

2.1.1. Talbot Effect

The operational principle of grating interferometry relies on a phenomenon known as the Talbot effect, which demonstrates a self-imaging characteristic. Talbot first observed this effect in 1836 using visible light, and later in 1881, Lord Rayleigh provided an analytical explanation for it. The Talbot effect describes the formation of “self-images” of regular patterns when illuminated by coherent radiation. Talbot noticed that when a periodic object with absorption properties is exposed to spatially coherent radiation, a "self-image" is formed at specific distances. This phenomenon occurs due to Fresnel diffraction and leads to the recurrence of a periodic wavefront at a specific distance referred to as the Talbot distance (d_T) [41, 42].

2.1.2 The Talbot-Lau Interferometer components

The Phase Grating. The first grating, labeled as G_1 with a period p_1, splits the X-ray beam in its primary diffraction orders, afterward interfering downstream and producing a periodic interference pattern with a rectangular shape. When a refractive object is present, this pattern undergoes lateral shifting. By analyzing this distortion, valuable details about the optical characteristics of the sample can be obtained.

The analyzer grating. The second grating, labeled as G_2 with a period p_2, is designed as a purely absorbing grating that corresponds to the period of the created interference pattern. The period of the fringes in the obtained pattern is so small that it often cannot be directly solved by the majority of high-resolution detectors, given the limitations of their field of view and pixel size. To overcome this limitation, an analyzer grating G_2 is used to convert the local position of the fringes into modulation of intensity.

The source grating. The third grating, and the one which gives the versatility of the technique and allows the use of this kind of interferometer with a conventional X-ray tube, is the source grating. To achieve interference effects and generate fringes with significant contrast, specific conditions regarding the transverse coherence of the wavefront need to be met. Actual X-ray sources are not perfect point sources and have a limited lateral size, leading to a phenomenon known as partial spatial or transverse coherence.

2.1.3. Key characteristics of Talbot-Lau Interferometer

The first essential characteristic of the Talbot-Lau Interferometer is the *angular sensitivity S*, which basically determines the dynamic energy range of the Interferometer. In this thesis, it is defined as the ratio between the period p_2 of the G_2 grating and the distance (D) between the G_1

and G_2 gratings. In essence, the angular sensitivity determines how small are the refraction angles that can be detected. The highest angular sensitivity is achieved in "symmetric" setups where the distances between gratings are equal and four times the Talbot distance (d_T), $L=D=4\cdot d_T$ and the periods of all the three gratings (G_0, G_1, and G_2) are the same $p_0=p_1=p_2$. To optimize the effective angular sensitivity, the object should be positioned as near as feasible to middle phase grating [16, 19]. The object magnification factor (M) is approximately $M\sim 2$ in symmetric setups. This means that the symmetric setup enhances the sensitivity to small angular changes, allowing for more precise measurement of refraction angles.

The second key parameter of a Talbot-Lau interferometer is the fringe *Visibility* or fringe contrast, *V*. The visibility of the micropattern quantifies the intensity change resulting from a pattern shift and is determined by the normalized difference between the maximum and minimum intensity of the pattern. The visibility is defined as:

$$V = \frac{I_{max} - I_{min}}{I_{max} + I_{min}}, \tag{2.2}$$

I_{max} represents the maximum intensity, and I_{min} represents the minimum intensity profile across the Talbot fringe pattern [17].

2.2. Data analysis for retrieval of the absorption, refraction, and scatter images

In addition to the previously described benefits, another significant advantage of grating phase contrast imaging is the ability to separate absorption, refraction, and scattering contributions to the X-ray signal, resulting in the acquisition of three different images [18, 19, 43, 44]. The first image is the conventional absorption image, which contains the X-ray attenuation within the object. The second image is the refraction or phase image, which highlights differential density variations or gradients. The third image is the scattering image, illustrating density variations at the micrometer scale. The refraction image significantly enhances the edges of the object, making it valuable for emphasizing tumor or lesion boundaries, among other applications. A supplementary image can be obtained by numerically integrating the refraction image, providing high sensitivity in detecting minor density differences within the object's bulk. These images can be obtained through the phase-stepping procedure or Moiré fringes. The following section briefly describes all analysis methods used in this thesis: phase stepping, Moiré fringe, and refraction enhanced.

Phase-stepping procedure. The prevailing approach for characterizing the interference pattern in a grating-based interferometer is the phase-stepping method, involving the lateral displacement of one of the gratings. The movement is performed in steps of a fraction of the grating

period, perpendicular to both the grating lines and the direction of the beam. This shifting process is performed across at least one complete interference pattern period, ensuring a minimum of three steps per period. At every position, an image is acquired. The grating scan varies the transmission of the interferometer as a function of the deviation angle, producing in each detector pixel a nearly sinusoidal intensity modulation curve. It is important to note that the period of the interference pattern is significantly smaller than the size of individual camera pixels. This method offers several advantages over the Moiré fringe analysis method. Firstly, it enables the retrieval of differential phase information independently at each pixel. Secondly, the analysis itself is straightforward, rapid, and dependable, providing an efficient means of interpretation [45, 44].

Moiré fringes. Another possibility for phase retrieving is the direct analysis of Moiré fringe images. One of its main advantages is the ability to extract all the necessary information from a single image, enabling single-shot experiments, useful in pulsed sources like XFELs or laser-based X-ray sources. Another advantage is eliminating the need for high performance actuators with nanometer-level resolution, typically required for phase stepping. Also, the three associated images can be extracted in principle, but the spatial resolution in one direction is limited at approximately the Moiré fringe period [46]. However, there are certain drawbacks associated with Moiré fringe analysis. It involves more complex analysis techniques, offers lower spatial resolution determined by the density of the Moiré fringes, and may exhibit more substantial phase wrapping effects [47].

Refraction enhanced. Furthermore, it is feasible to capture refraction effects in a single exposure, maintaining the complete spatial resolution of the imaging system. This approach is known as "Refraction Enhanced" (RE) imaging. In the RE setup, the gratings are positioned at the midpoint of the quasi-linear segment of the phase stepping curve. This positioning allows the angular deviations caused by a refraction to be directly visible in the raw interferogram [16]. Notably, with an extremely sensitive interferometer, as the ones proposed in this thesis, this technique opens up the potential for significantly reducing the required dose or exposure time in phase contrast imaging.

Each proposed data collection and analysis technique has advantages and can be suitable for clinical implementation in different conditions. Chapter 3 presents the results of a proposed breast radiography interferometric system with a conventional X-ray source, enabling all the techniques described in this section. However, the idea of optimizing and developing the system for laser-based breast radiography is also discussed, motivated, and argued with XWFP calculation and simulation in Chapter 4.

Chapter 3. Experimental results

Even though grating interferometry has undergone extensive research because of its massive potential in medical field applications and is near to clinical implementation, there is still room for improvement to get to the maximum from this technique. This chapter presents the experimental results on ultrahigh sensitive phase-contrast imaging obtained in the XIL laboratory from ELI-NP and Johns Hopkins University, Department of Physics and Astronomy in Baltimore, USA. It focuses on depicting the details of developing and optimizing an interferometric radiography method for the breast but also shows and discusses possible ways of implementing this technique for cardio-pulmonary application.

3.1. Experimental demonstration of ultrahigh sensitivity Talbot-Lau interferometer for low-dose breast radiography

In this subchapter, we address two of the main challenges towards clinical implementation - limited angular sensitivity and high radiation dose - specifically in the context of interferometric radiography of the breast. We propose using ultrahigh angular sensitivity Talbot-Lau interferometers with gratings having periods of a few micrometers and lengths of several meters. Furthermore, to facilitate the practical implementation and reach the full potential of ultrahigh sensitivity interferometric mammography, we suggest replacing the conventional X-ray tubes with X-ray sources powered by high-intensity lasers that can deliver an adequate number of photons over long distances within acceptable exposure times for mammography (up to a few seconds).

3.1.1. Materials and Methods

The experimental configuration comprises three main components: an ultrahigh sensitivity interferometer, a high-power conventional X-ray tube, and an in-house-built detector. The interferometer was constructed on a 6-meter-long optical table, and the entire laboratory setup is situated on the vibration-isolated experimental area platform provided by ELI-NP. Figures 3.1 a)

and 3.1 b) show a graphic illustration of the experimental setup and the layout of the ultrahigh sensitivity interferometry at the ELI-NP X-ray Imaging Laboratory (XIL).

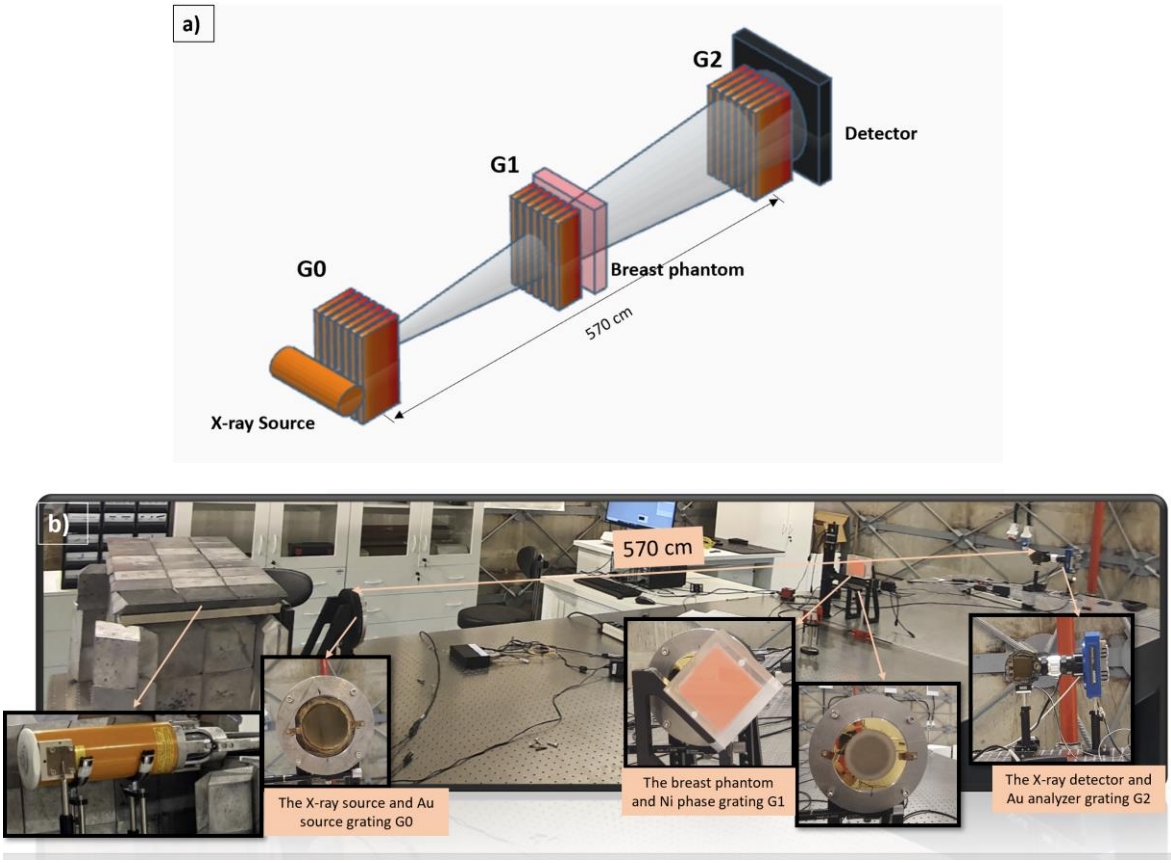

Figure 3. 1. Ultrahigh sensitivity long Talbot-Lau interferometer for interferometric breast radiography. a)Schematic representation. b) Photograph of the table-top laboratory setup for the study of interferometric breast radiography, together with close-up views of the main components.

Characterization of the ultrahigh sensitivity Interferometer. As explained in detail in Chapter 2, the Talbot-Lau interferometers have two main key parameters: angular sensitivity and fringe visibility. A detailed analysis of the two parameters is needed to fully characterize and optimize this kind of setup.

Angular sensitivity. The primary characteristic of the Talbot-Lau setup is its angular sensitivity, defined as the interferometer period divided by the intergrating distance. This sensitivity has an essential function in determining the dynamic range of the instrument. Tests using interferometers ranging from approximately 4 to 6 meters were conducted. In the context of this experiment on phantom mammography, a 5.7-meter-long interferometer was utilized, resulting in a remarkable nominal angular sensitivity of 0.87 μradians. To validate this sensitivity experimentally, the Moiré fringe shift generated by an acrylic resin prism positioned at 45° in the beam path and designed to deflect X-rays by approximately 1 μrad at~30 keV was measured.

Fringe visibility. In the interferometer built for this experiment, the visibility curve breaks as an energy function and exhibits numerous peaks (approximately 100), forming a quasi-continuous distribution across the X-ray spectrum emitted. In this case, the calculation includes the finite height of the G_1 and G_2 bars. The spectrally averaged visibility obtained from the computation is relatively high, approximately 15-16%. Furthermore, due to the presence of multiple high-frequency peaks in the visibility curve, the average fringe contrast of the interferometer with a broad X-ray spectrum no longer varies with the Talbot distance but remains constant.

Dose calculation.

A particular dose calculation protocol was developed because the method proposed in this thesis is not implemented at the clinical level, so there is no existing methodology for approximating the mean glandular dose. Similar to the mammography dose protocols [48], the proposed methodology for the presented experiments in this thesis includes a measurement with an ionization chamber of KERMA in air and simulation and a calculation with FLUKA to determine the necessary conversion factor.

The measurements were conducted along the X-ray beam axis, positioned at a length of 285 cm from the focal point of the X-ray tube. A 2 mm diameter collimator was utilized to restrict the X-ray radiation at the source. The measurements were carried out using a UNIDOS Secondary Standard Dosimetry System and a TN23342 plan parallel chamber manufactured by PTW. Furthermore, to calculate the mean glandular dose deposited in the mammary gland, the measured incident air KERMA was multiplied by a conversion factor obtained from Monte Carlo simulations and computations using the FLUKA code [49, 49, 50]. The conversion factor was determined by considering the actual geometry of our interferometric setup, X-ray spectrum, filtration, and utilizing a standard numerical breast phantom with a total thickness of 5 cm. The calculations employed tissue compositions recommended by the ICRU (report 44 1989). The conversion factor for our specific configuration was 0.464 at 40 kVp.

3.1.2. Results and Discussion

3.1.2.1. Phase stepping results with ultrahigh sensitivity interferometer for breast radiography

The results obtained through a phase-stepping procedure of 16 steps of 0.3 μm and 32 seconds exposure time per each step using a 400 μm source spot are depicted in Figure 3.2, Figure 3.3, and Figure 3.4, and they confirm the exceptional sensitivity of the proposed interferometric setup for breast radiography. A series of fibers, calcification, and tumor-like masses from the Gammex 156 accreditation mammography phantom were imaged. For the purpose of comparing

these results with conventional mammography and to highlight the considerable potential of this technique, absorption images of the same objects using a typical-like mammography setup were acquired. This setup involved a source-detector distance of 65 cm, a magnification of approximately M~1, and a tungsten anode tube operating at 28 kVp with 50 µm Rh filtering. The exposure was 100 mAs, and image acquisition was performed using the same lens-coupled CsI detector, resulting in a glandular dose estimated at ~ 1 mGy. The estimated dose is obtained by scaling the 100 mAs exposure used in this experiment to the 160 mAs used in reference [51]. It is important to note that the images obtained with this setup, referred to as "absorption mammography" in the following figures, were not acquired using a clinical examination mammography system.

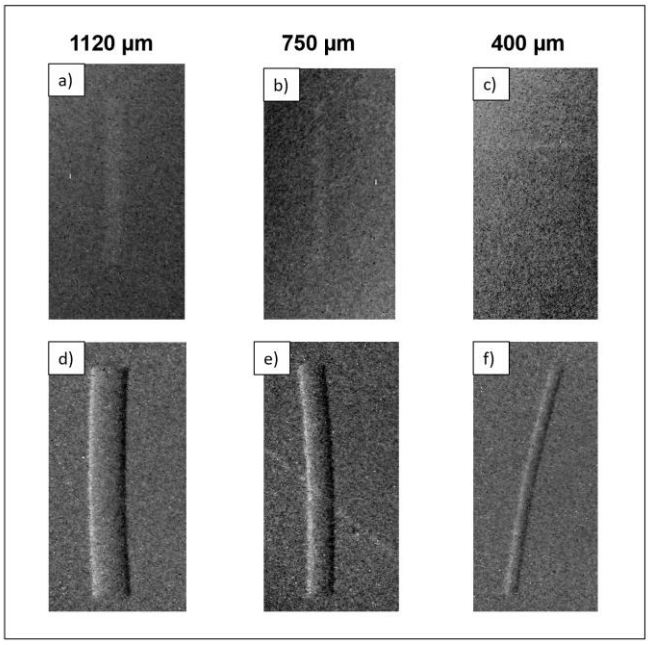

Figure 3.2. Conventional mammography images (a, b, c) at an estimated dose of 1 mGy and interferometric mammography phase images (d, e, f) of fibers in the GAMMEX 156 phantom, obtained at a dose of 2.73 mGy. The object size is indicated above each image. The intensity scale in the conventional images is 90-105% of the mean count value, and the scale in the phase images is from -1 to +1 microradian.

The visibility of the objects is significantly enhanced in the refraction and dark-field images relative to the ones from conventional mammography. Remarkably, even the smallest fiber with a diameter of 400 µm and the smallest specks simulating calcifications with a diameter of 160 µm are detected (figure 3.3), despite the spatial resolution of our M~2 setup with a 400 µm source spot being approximately 250 µm. This suggests that the ultrahigh sensitivity PXI technique can potentially detect breast tissue anomalies, even when using a large spot X-ray tube and a higher magnification.

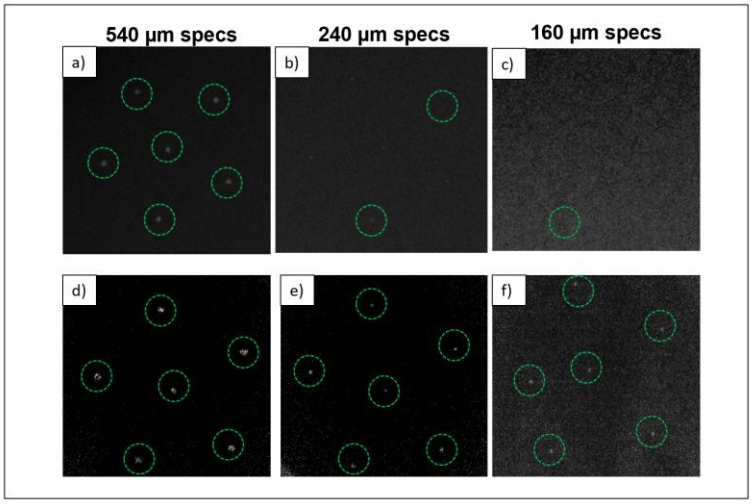

Figure 3. 2. Conventional mammography images (a-,c) and interferometric mammography dark-field images (d-,f) of specs simulating calcifications. The object size is indicated above each image. The intensity scale in conventional mammography images is 90-105% of the mean count value. The scale in the dark-field image is between 35-42% of the fringe contrast of the stepping curve (calculated as the ratio between the average value of the stepping curve in the presence of the object and the visibility of a reference scan).

Furthermore, all the tumoral masses in the phantom were easily discernible in the dark-field images acquired using the ultrahigh sensitivity setup. In contrast, only masses with a thickness above 750 µm could be detected in the conventional mammography setup (see Figure 3.4). However, it is essential to emphasize that the dark-field signal from the tumoral masses is likely increased due to the presence of X-ray scattering material, which may not necessarily occur in actual breast tissue.

The results presented in this work represent a significant improvement not only compared to conventional mammography but also compared to previously reported interferometric mammography setups. For example, a direct comparison can be made between Figures 3.2, 3.3 and 3.4 and Figures 2f, 2g, and 2h from reference [51]. The results in reference [51] were obtained using an asymmetric interferometer of 1.5 m length, operating at 40 kVp, with a dose of 2.07 mGy, and the same Gammex 156 phantom. The comparison demonstrates a substantially increased visibility for larger fibers and the ability to detect the smallest fibers and calcifications in our case, which were not detected in reference [51] using either conventional or interferometric mammography.

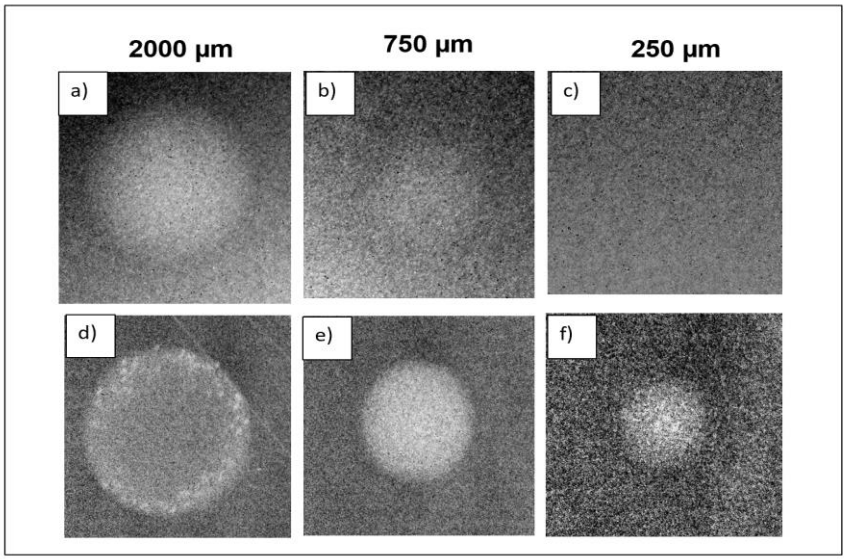

Figure 3. 3. Conventional mammography images (a-c) at 1 mGy and interferometric dark field images (d-f) of tumor-like masses obtained at a dose of 2.73 mGy. The intensity scale in the conventional mammography images is 90-105% of the mean count value, and the scale in the dark-field images is 25-30% of the fringe contrast of the stepping curve. The thickness of the masses is given above the images.

Lastly, one of the goals of the proposed interferometric breast radiography is to minimize the radiation dose. While the results demonstrated improved sensitivity and visibility, they were obtained at a relatively high radiation dose of 2.73 mGy. To provide an initial evaluation of ultrahigh sensitivity interferometric mammography at a reduced dose, experiments were conducted by gradually decreasing the number of phase steps and the exposure time for each step.

Figure 3.5 presents the results obtained for a 750 µm fiber from the mammographic phantom, demonstrating the ultrahigh sensitivity interferometry capability even at a low dose of 0.32 mGy. In contrast, the fiber is completely imperceptible in the absorption images obtained from the same phase stepping data set.

Furthermore, in Figure 3.5, an estimation of the CNR (contrast-to-noise ratio) in the fiber refraction angle images using a method similar to that described by Eggl et al. in Scientific Reports [52] is provided. The CNR is calculated as the difference between the mean image value in a signal area S and the mean image value in a background area B, divided by the standard deviation of the values in the background area B. In Figure 3.5, the width of the signal area S was selected to extend from the edge of the fiber to the middle of the fiber, and the height was chosen to be several times larger. The CNR in the phase contrast images ranges from a remarkable 5.5 at the highest dose to 1.8 at the lowest dose. The CNR in the corresponding absorption images cannot be evaluated, except that it is much less than 1, because there is essentially no visible image of the fiber left.

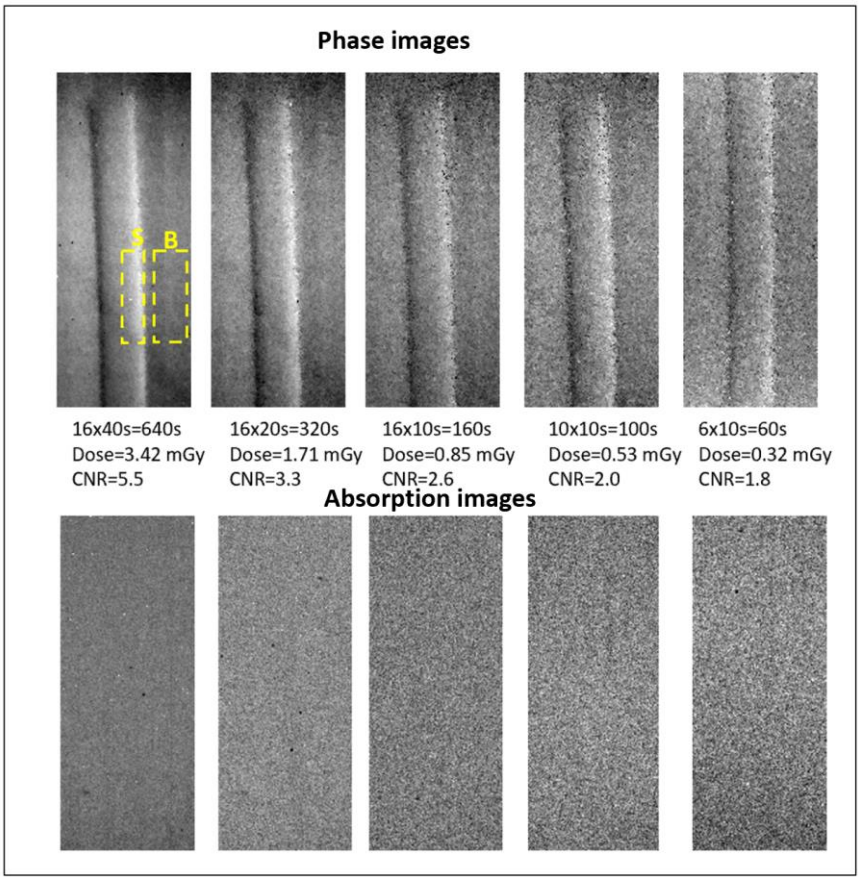

Figure 3. 4. Phase images from interferometric breast radiography and the corresponding absorption images of 750 µm fiber *in the GAMMEX 156 phantom, obtained at reduced doses by performing the phase stepping procedure and Fourier analysis with progressively fewer steps and shorter exposure times. The number of steps, exposure time, dose, and contrast-to-noise ratio (CNR) is shown under each image. The intensity scale in the absorption images is 90-105% of the mean count value, and the scale in the phase images is from -1 to +1 microradian.*

3.1.2.2. Moiré results with ultrahigh sensitivity interferometer for breast radiography

Furthermore, in Figure 3.6, results obtained with the single exposure Moiré technique for fibers of 1156 µm, 1112 µm, and 750 µm are shown. The acquisition time for each image was 360 seconds, and the mean glandular dose was~1,92 mGy. The frequency of the fringe was kept high for better visual identification. Even so, in the case of the smaller fibers of 1112 µm and 750 µm, the edges of the fibers start to fade, and identification is difficult to be done. In the case of actual tissue, this method will be hard to implement because the structure of the tissue is complex, and small perturbations of fringes corresponding to minor abnormalities are challenging to identify.

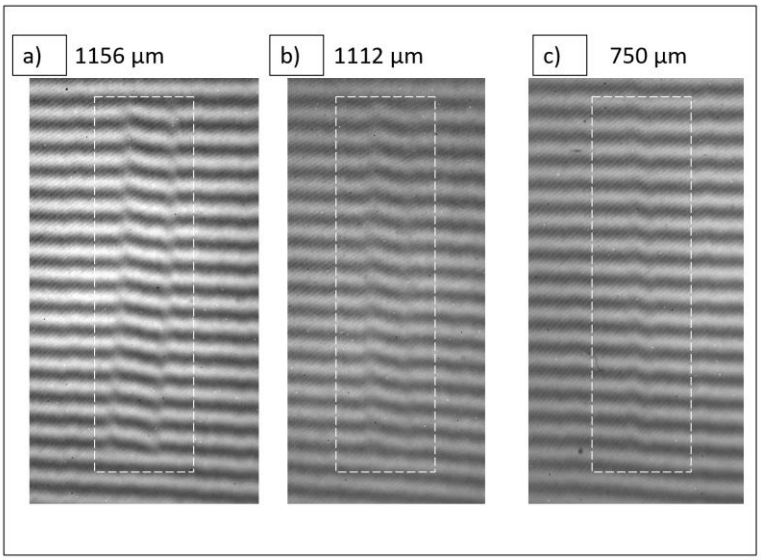

Figure 3. 5 Single exposure Moiré interferometric breast radiography images of fibers in the GAMMEX 156 phantom, obtained at a dose of 1.92 mGy. The object size is indicated above each image.

3.1.2.3. Refraction-enhanced results with ultrahigh sensitivity interferometer for breast radiography

Ultrahigh sensitivity refraction-enhanced imaging results are illustrated in Figure 3.7, where the interferometer was put in the refraction-enhanced position, the most sensitive position to phase changes [16, 53]. The acquisition time for each image was 360 seconds, and the dose was 2.73 mGy.

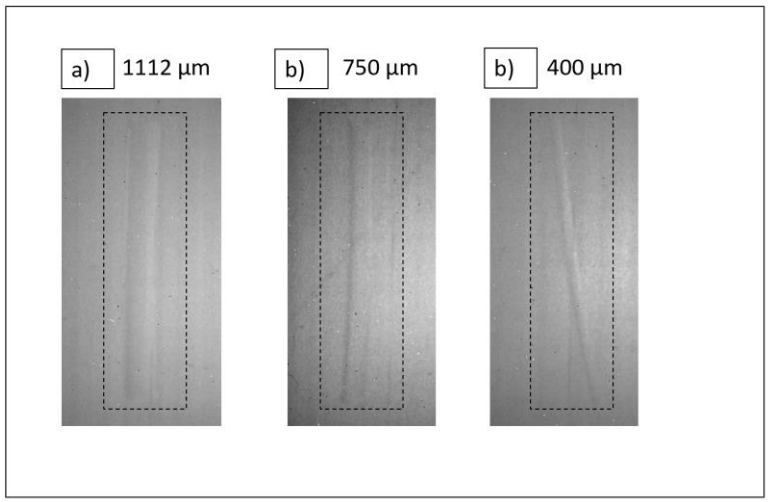

Figure 3.7. Single-shot refraction-enhanced images obtained with the proposed interferometric breast radiography setup at a normal incidence of fibers in the GAMMEX 156 phantom. The images were obtained at position RE on the stepping curve (image 2.7 – Chapter 2) at a dose of 2.73 mGy.

As in the case of Moiré interferometric breast radiography images, the larger fiber of 1120 µm can be easily identified, but the smaller ones of 750 µm and 400 µm start to fade. For a better visualization in the case of this method, higher contrast is necessary. The results obtained through this technique with a higher contrast will be presented in the next section of this chapter and will highlight the importance of fringe visibility for the proposed method.

3.1.2.4. Results with ultrahigh sensitivity interferometer on a breast tumor sample

After optimization of the setup on an accredited mammographic phantom, tests on real breast tumor samples embedded in paraffin were done. The cancer samples are from IOB Histoteca, and the results obtained on mammary carcinoma, grade 1 sample (well-differentiated), are shown in Figure 3.8. The images were obtained at 40 kVp and 10 mA with a focal spot of 400 µm, performing a phase-stepping procedure of 16 steps of 0.3 µm on two periods. Histopathological images for the same sample at different magnifications are shown to compare and validate the results.

Even though these samples are not truly representative of live breast tissue, being dried and embedded in paraffin, so different from the natural structure of an actual tumor inside the breast, quite striking results were obtained in the darkfield contrast channel. As shown in Figure 3.20 a), in the absorption image, the tumor is entirely invisible; just the stripes of the plastic holder of the paraffin are visible. In the darkfield image, all the tumor region is visible and accessible for identification, with some ramification inside the adipose tissue. In phase image, because of the dryness of the tissue and irregularities on the surface of the paraffin, the interesting signal is almost erased, but still, there are some signs of possible tumor identification.

The microscopic histopathological images confirm the results obtained with the phase-contrast imaging technique even for this kind of sample and indicate that for fresh tissue samples, the results might be more accurate with more information available to extract. If the cancer tissue scatter effect will be confirmed in live tissues, ultrahigh sensitivity dark-field imaging could bring a significant breakthrough in medical imaging.

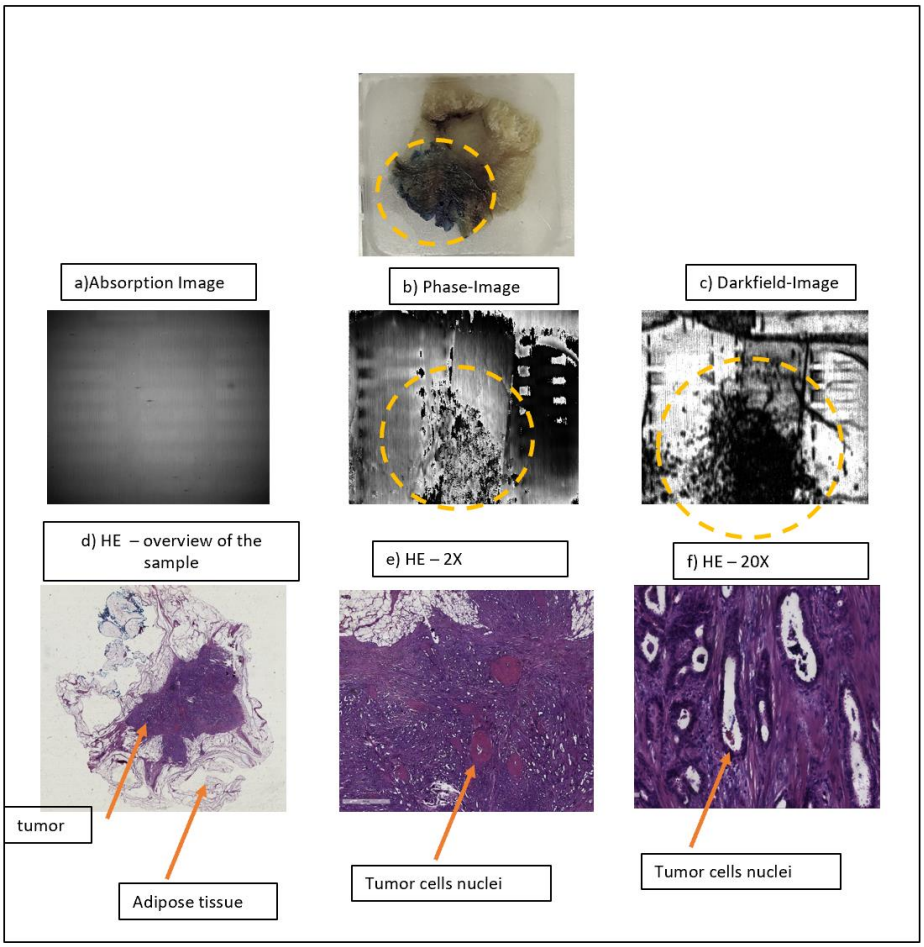

Figure 3.8. a) Absorption image, b) phase image, and c) scattering or dark field image of a breast tumor sample in paraffin obtained at a total exposure time of 1920 seconds corresponding to a phase stepping procedure of 16 steps of 0.3 µm and 120 seconds per each step. d), e), f) microscopic histopathological images showing the presence of cancer as in the images obtained through the proposed technique from the XIL laboratory

The results depicted in this subchapter confirm the possibility of ultrahigh sensitivity and dose economy with the proposed setup. The visibility of objects simulating cancerous formations is strongly increased in the refraction images over the attenuation ones, even at a low dose of 0.32 mGy. Notably, the smallest fiber of 400 µm diameter and calcifications specs of 160 µm are detected, even though the spatial resolution at the object of our M ~2 setup with a 400 µm source spot is only ~250 µm. These experiments on a mammography phantom illustrate the capabilities of the proposed method and open the way toward laser-based interferometric mammography. There are also ways to decrease the dose below the used values.

A part of the work involved in this subchapter was published in Safca, N., Stutman, D., Anghel, E., Negoita, F., & Ur, C. A. (2022). Experimental demonstration of ultrahigh sensitivity Talbot-Lau interferometer for low dose mammography. Physics in Medicine & Biology, 67(23), 23NT01.

3.2. Ultrahigh Sensitivity Glancing Angle Interferometer for Low-Dose Breast Radiography

In this section of the thesis, the concept previously introduced in Chapter 3.1, where the imaging results on a mammography phantom from a 5.7 m long Talbot-Lau Interferometer employing 2.4 μm period gratings at normal incidence are presented, with sensitivity better than 1 μradian, is further developed. This work investigates new enhancements to the performance of the interferometer, focusing on medical applications such as mammography with reduced doses and increased sensitivity. The utilization of very long setups exceeding 5 meters, combined with micro period gratings, enables the capability of adjustments in the length of the grating-based Talbot-Lau interferometry without impacting the visibility.

3.2.1. Materials and Methods

The improvement to the initial setup consists of enhancing the fringe visibility at high X-ray energy while preserving the ultrahigh angular sensitivity. This is accomplished by implementing a Glancing Angle Interferometer configuration [54, 55] of the 5.7 m long Talbot-Lau Interferometer with 2.4 μm period gratings. The Lewis observations from 2004 and the measurements and calculations done in Chapter 3 demonstrate that PXI at higher X-ray energy, where soft tissue absorption decreases, can considerably reduce the radiation delivered to the patient. However, the fringe visibility at higher X-ray energies is limited by the practical thickness of the absorber (typically gold) present in the G_0 and G_2 gratings [56].

To maintain the ultrahigh sensitivity of the setup while simultaneously increasing the fringe visibility, given the current limitations in grating fabrication capabilities for higher energies (approximately above 25 keV), a Glancing Angle Interferometer with an incidence angle α of 45° was constructed. By implementing this configuration, the effective thickness of the gratings was increased by a factor of $1/\sin(\alpha)$, which is approximately 1.4. This caused a higher absorption of the X-rays in the gratings and, consequently, an overall improvement in the visibility of the interferometer fringes.

With these two enhanced characteristics, improved images using the phase-stepping method at low doses of 1.68 mGy and 0.43 mGy and the refraction-enhanced technique at a dose as low as 0.1 mGy were obtained. In this method, the interferometer is positioned at the point where it is most sensitive to changes in refraction angles. According to the previously mentioned studies [16, 53], this point is achieved at the midpoint of the quasi-linear portion of the phase

stepping curve, where the intensity variation per refraction angle change is maximized. This position was used to obtain images of objects of medical relevance using the same mammographic accreditation phantom.

Dose improvement with GAI. To estimate the dose, the method described in Chapter 3 was used. All the results were obtained at 40 kVp. The mean glandular doses range from 0.46 mGy to 0.1 mGy for the same fibers from the mammographic phantom of 1120 µm, 750 µm, and 400 µm. These results were obtained using different exposure times and employing either the phase-stepping or refraction-enhanced technique.

3.2.2. Results and Discussion

3.2.2.1. Phase-stepping results with GAI interferometer for breast radiography

This part of the thesis is focused on imaging the smallest fibers from the Gammex 156 accreditation mammography phantom to showcase the capabilities and characteristics of the proposed method for medical applications. Figures 3.9 and 3.10 illustrate the results obtained using the phase-stepping procedure specifically for the targeted fibers measuring 1120 µm, 750 µm, and 400 µm. These images demonstrate the ability of our method to resolve and visualize fine details of the fibers with high precision and a relatively low dose.

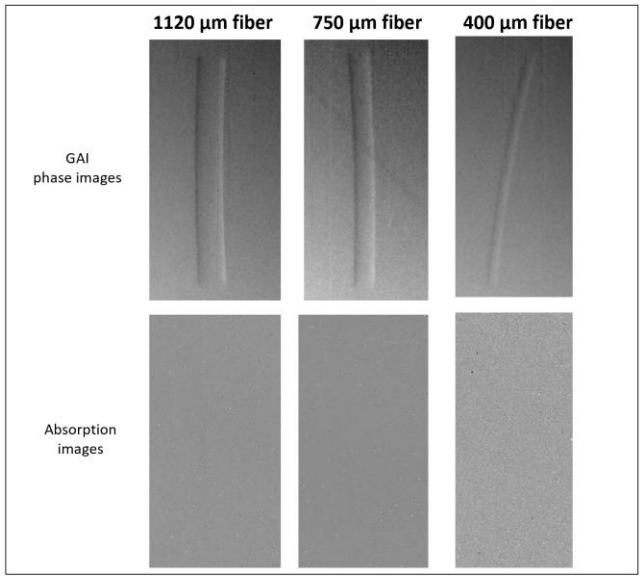

Figure 3. 9. Interferometric radiography images of 1120 µm, 750 µm, and 400 µm fibers from the Gammex phantom and the corresponding attenuation images obtained through a phase stepping procedure of 16 steps of 0.3µm and 20 seconds per each step (a total exposure of 320s), 40 kVp, 15 mA, and a mean glandular dose of 1.68 mGy. The contrast-to-noise ratio CNR is between 1.9 and 2.4. The intensity scale in the attenuation images is 85-90% of the mean count value, and the scale in the interferometric images is from -1 to +1 microradian.

Moreover, one of the critical aspects for the clinical implementation of interferometric breast radiography is the optimal balance between imaging performance and the radiation dose. Even though the results in Figure 3.18 were already obtained at a relatively low radiation dose of 1.62 mGy (the dose in conventional mammography can reach range between 3-5 mGy), because of the improvement in fringe contrast, there are ways to decrease the dose further while maintaining the high sensitivity of the system. In the first phase, good images of the tumor-like objects at a lower dose of 0.42 mGy were obtained by systematically decreasing the count of phase steps to 5 steps per phase stepping procedure. Tests on tumor-like objects were done, and the limit of the system with this procedure, considering the ratio between dose and image quality, was reached at five steps per procedure and a total mean glandular dose per image of 0.42 mGy. Going lower than these values compromises the quality of the performance of the interferometer. The results obtained with these adjustments are shown in Figure 3.24.

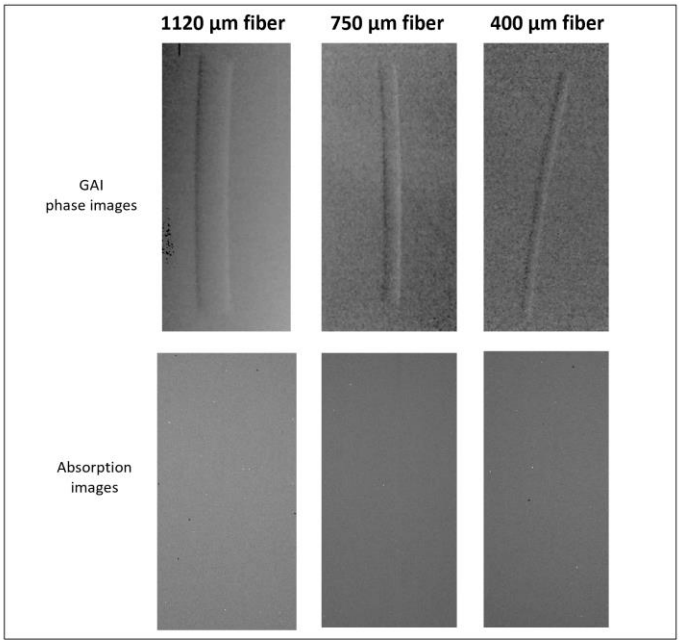

Figure 3. 10. Images corresponding to a phase stepping procedure of 5 steps of 0.48 µm and 16 seconds per each step (a cumulative exposure duration of 80 seconds), 40 kVp, 15mA, and a mean glandular dose of 0.42 mGy. The contrast-to-noise ratio CNR is between 1.8 and 2. The intensity scale in the attenuation images is 85-90% of the mean count value, and the scale in the interferometric images is from -1 to +1 microradian.

As a result of the increased fringe visibility of 20%-22% in the Glancing Angle Interferometer (GAI) geometry as compared to approximately 15% in the normal incidence configuration, the Contrast-to-Noise Ratio (CNR) improved (e.g., for the fiber of 750 µm 1.9 to 2.4 at an exposure of 80 s). The enhanced contrast, combined with the maintained high angular sensitivity of 0.82 µradians, resulted in improved visibility of the tumoral fiber, even at a very low dose. The edges of the objects appeared well-defined and sharp, even at a dose as low as 0.42

mGy in the interferometric radiography, while these margins are entirely invisible in the associated absorption images obtained from the phase stepping procedure.

3.2.2.2. Refraction-enhanced results with GAI interferometer for breast radiography

Another way to decrease the dose while maintaining an acceptable quality of the images is the refraction-enhanced method. Figure 3.11 illustrates the effect of the "refraction enhancement" method achieved through a single-shot image obtained having simultaneously high angular sensitivity and medium to high interferometer visibility. These images clearly demonstrate the significance of fringe contrast in the refraction-enhanced technique and allow for a direct comparison with the normal incidence approach.

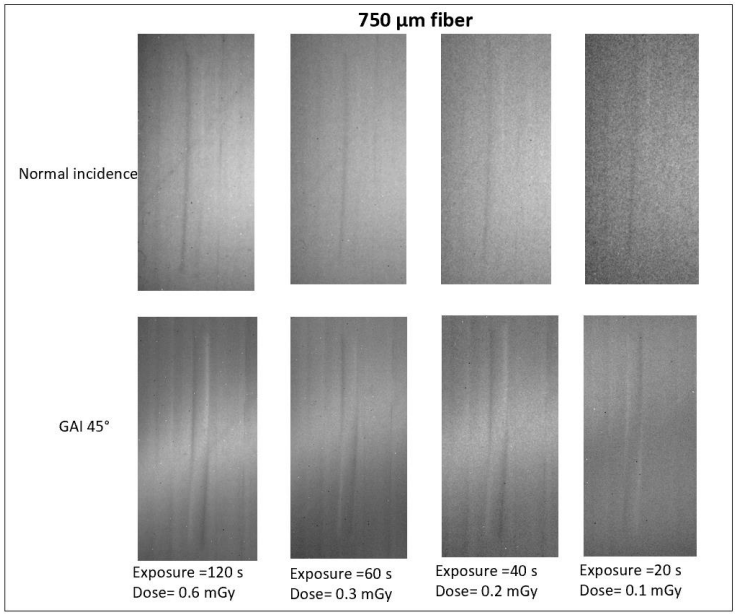

Figure 3.11. Single-shot refraction-enhanced images obtained with a setup at normal incidence and with the GAI interferometer from the XIL laboratory of 750 µm fiber in the GAMMEX 156 phantom. The images were obtained at position RE on the stepping curve at reduced doses of 0.6 mGy to 0.1 mGy by decreasing the exposure times.

In the refraction-enhanced images obtained using the Glancing Angle Interferometer (GAI), some "moving shadows" can be seen. These are caused by residual Moiré fringes from the GAI system. While achieving Moiré-free images at normal incidence was possible, aligning and removing Moiré fringes in very long and ultrahigh sensitivity GAI interferometers are more challenging. Finding a solution to eliminate these shadows is necessary to improve the results, as they can interfere with the diagnostic process. There is a big chance that they cannot be eliminated but only reduced because when the source G_0 is included, there is an unavoidable asymmetry in

the GAI setup. A G_0-less setup obtainable with a laser-based X-ray source might solve this problem. However, despite this effect, the fiber remains visible even at a low dose of 0.1 mGy in both configurations. In the normal incidence setup, the fiber starts to disappear, and the margins blur at doses starting with 0.3 mGy due to the lower contrast of the interferometer and the moderate spatial resolution of the system (250 μm).

In this subchapter of the thesis, the construction and performance of a 584 cm laboratory glancing angle interferometer (GAI) operated at a 45° angle, achieving an unprecedented angular sensitivity of 0.82 μradians with 22% fringe visibility, were presented. The GAI setup was used to acquire images of structures that simulate malignancies at a mean energy of 30 keV, enabling both phase stepping procedure and refraction-enhanced method. The findings illustrate that the suggested approach provides valuable and detailed information about the objects, being capable of providing early diagnosis at a low radiation dose, starting with 0.42 mGy for the phase-stepping method and decreasing to 0.1 mGy in the case of the refraction enhanced one.

There is still room for improving the results and reaching the full potential of phase contrast imaging. A better resolution which can be achieved with an X-ray laser-based source, is the key towards this purpose. These new X-ray sources have high spatial coherence, a spot size of 1-2 μradians, and can provide sufficient photons at long distances within the exposure times acceptable in mammography (up to a few seconds). Chapter 4 presents in detail the motivation and results of computation done in XWFP for laser-based PXI.

3.3. Perspective on using ultrahigh sensitivity Talbot-Lau interferometer for cardio-vascular and pulmonary applications

This Chapter presents the capabilities of Talbot-Lau interferometry for other medical applications. The focus is on cardio-pulmonary application, primarily on arterial plaque identification. Results obtained on a human artery and a rat heart are presented.

As discussed, one of the significant strengths of PXI is its ability to provide multiple types of image contrast. By separating the contributions of absorption, refraction, and scattering to the X-ray signal, PXI can generate three different images: the conventional absorption image, the phase image highlighting density gradients and edges, and the darkfield image depicting density variations at the microscale. The phase image, in particular, enhances object boundaries and can be helpful in highlighting tumors or lesion boundaries. Studies, such as the experimental ex-vivo research conducted by Holger Hetterich et al. [57], have explored the use of phase-contrast

computed tomography for characterizing atherosclerotic plaques. The results demonstrate the capability of phase contrast tomography to differentiate critical components of plaques, including the fibrous layer and calcified structures. The present subchapter highlights the potential of simple phase contrast radiography, without tomographic reconstruction, in detecting plaque calcification, lipids, and potentially cholesterol crystals. This suggests that PXI techniques, even in simpler forms, can identify and characterize atherosclerotic plaques, providing valuable information for diagnosing atherosclerosis.

3.3.1. High sensitivity interferometer for atherosclerosis diagnosis

The work presented in this section was conducted at Johns Hopkins University, Department of Physics and Astronomy in Baltimore, USA, and aimed to illustrate the ultrahigh sensitivity of PXI at 20-40 keV, clinically relevant energies in medical applications. The specific focus of the experiment was on utilizing this technique to identify atherosclerosis, a common and significant medical condition. The aim was to overcome the limitations of conventional imaging techniques by using the unique capabilities of phase contrast imaging, such as enhanced contrast and improved spatial resolution for soft tissues. The potential of this technique to detect atherosclerotic plaques, including components like plaque calcification, lipids, and cholesterol crystals, was explored.

3.3.1.2. Results and Discussion

The obtained results are shown in Figure 3.12. In the absorption image (a), which represents the standard X-ray image, no detailed information about the structure of the artery walls or the reference structure is observed. This image, most probably, primarily highlights the presence of lipid tissue and macrocalcifications resulting from the plaque. It cannot provide a clear visualization of the arterial structure.

On the other hand, in phase image (b), the structure of the artery walls, the reference structure of the soda straw, and the macrocalcifications are well-defined and distinguishable. The typical refraction angles in the phase image are of the order of 0.1 microradians. This high sensitivity to phase variations allows for enhanced visualization of subtle structural details that are not apparent in the absorption image. Additionally, the darkfield image reveals additional information not observable in the absorption and phase images. In the dark field image, tiny structures within the fatty mass and on the artery wall become visible aside from the macrocalcification. This is because these small structures are believed to be cholesterol crystals, which serve as early indications of thrombosis and atherosclerosis. Importantly, these structures

appear exclusively in the darkfield image and are not discernible in the absorption image, indicating the presence of a low-Z scattering material. This distinction suggests that these micro-structured low atomic number substances can be effectively identified and analyzed using the proposed method.

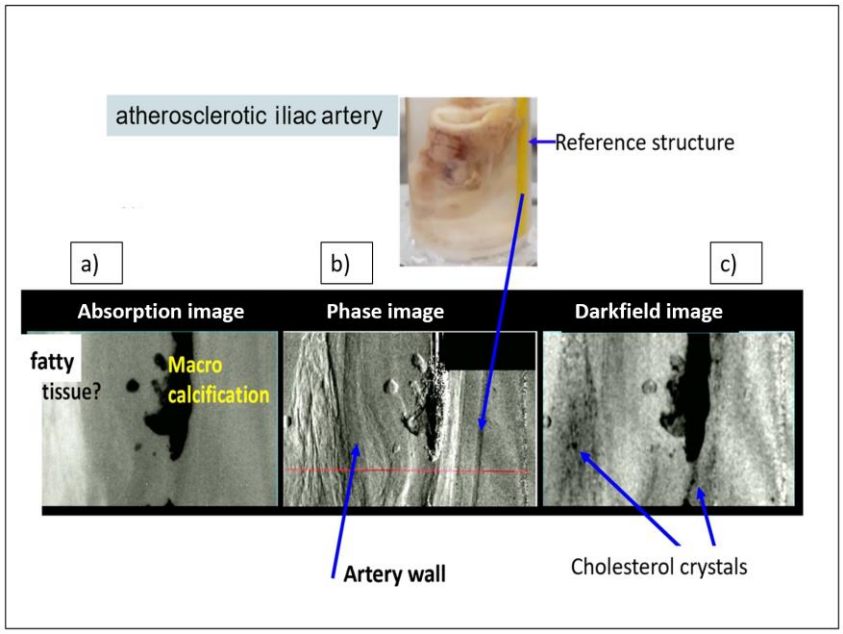

Figure 3.12. Results with high sensitivity interferometer on a human atherosclerotic iliac artery sample in formalin obtained with the Talbot-Lau set-up. a) Absorption image. b) Phase image. d) dark field image

By leveraging the capabilities of PXI, as demonstrated in this section, it may become possible to screen for early detection of atherosclerosis, a prevalent medical condition associated with significant health risks. The improved visualization of arterial structures, macrocalcification detection, and identification of micro-structured substances like cholesterol crystals offer promising early diagnosis and intervention opportunities. Therefore, the choice of the Talbot order, interferometer length, grating periods, and source size should be optimized to achieve high interferometer performance and be suitable for the chosen application.

A part of the work involved in this subchapter was published in Safca, Nicoleta, et al., "PERSPECTIVE ON USING TALBOT-LAU X-RAY PHASE CONTRAST IMAGING FOR ATHEROSCLEROSIS DIAGNOSIS." University Politehnica Of Bucharest Scientific Bulletin-Series A-Applied Mathematics And Physics 83.3 (2021): 257-266.

3.3.2. Experiments with ultrahigh sensitivity interferometer on a rat heart sample

Furthermore, to advance the studies on the cardio-vascular direction, experiments with an ultrahigh sensitivity Talbot-Lau interferometer at normal incidence having better than 1 μm angular sensitivity were conducted on a sample of rat heart immersed in formalin. The detector, the gratings, and the X-ray source are the same as the ones used and presented in Subchapter 3.1. The results are depicted in Figure 3.13 and confirm the capability of PXI in cardiac applications. The images were obtained at 30 kVp with 2 mm of Aluminium and medium energy calculated with Spekcalc of ~ 25 keV (design energy of the setup). The fringe contrast was 17%, and a phase-stepping procedure of 16 steps of 0.3 μm and 120 seconds per step was conducted to obtain the images.

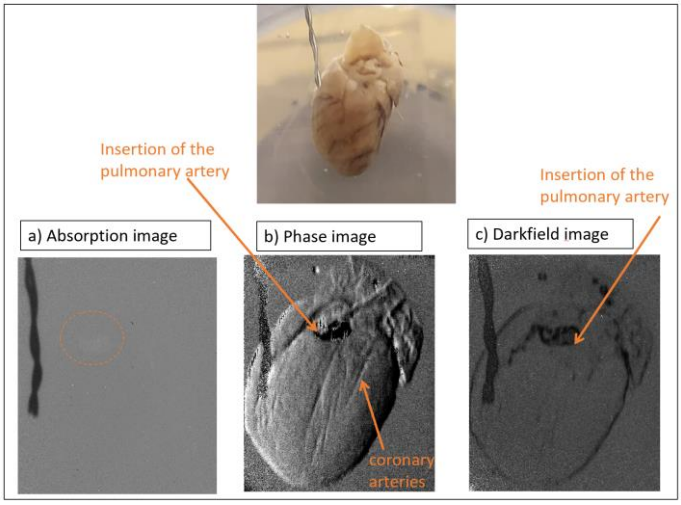

Figure 3. 13. a) Absorption image, b) phase image, and c) dark field image of a rat heart immersed in formalin obtained at a total exposure time of 1920 seconds corresponding to a phase stepping procedure of 16 steps of 0.3 μm and 120 seconds per step.

In Figure 3.13 a) representing the absorption image, the heart is invisible; maybe just a shadow of the opening of the insertion of the pulmonary artery is slightly visible. On the other hand, in the phase image, the entire heart is perceivable, the walls are well-defined, and even the coronary artery from the surface of the heart can be identified. The pulmonary artery insertion is clearly identified in both phase and darkfield images.

The findings presented in this section underscore the significant potential of the proposed method for potential cardiovascular applications and emphasize the need to improve the performance of the technique further and optimize it depending on the application.

Chapter 4. Towards laser-based ultrahigh-sensitivity and low-dose medical imaging

PXI has the prospective to improve the medical imaging diagnostic sector by offering greater sensitivity to soft tissue lesions or abnormalities in comparison to conventional absorption contrast X-ray imaging. One method particularly suitable for clinical use is the grating interferometry method. The studies conducted at the XIL laboratory and John Hopkins University and presented previously in Chapter 3 demonstrate that by employing interferometers with micrometer-period and meter-long dimensions, the phase sensitivity can be significantly enhanced, and dose reduction in medical imaging applications like mammography or plaque identification is possible. Unfortunately, conventional X-ray tubes do not provide the necessary X-ray flux for clinical imaging for such long interferometers. Alternatively, lasers of the 100-terawatt (TW) class can generate highly focused and intense X-ray sources, making them ideal for achieving high sensitivity in medical interferometry. In this Chapter, the essential characteristics of X-ray sources required for clinical interferometry are discussed, together with a comparison between the advantages and disadvantages of betatron and inverse Compton scattering sources. Practical considerations involved in laser-based interferometric medical imaging are also addressed.

4.1. Potential advantages and requirements of X-ray sources generated by lasers for medical interferometry

X-ray sources generated by lasers have the potential to serve as bright and directional microfocus X-ray sources, which could be highly suitable for achieving high sensitivity and low-dose medical interferometric imaging. Several reasons support this claim:

- Medical imaging requires a substantial X-ray output within a short period. Conventional mammography, for example, requires a fluence of approximately 10^7 photons/mm² over the breast area in just 1-2 seconds. Considering the average size of a compressed breast (around 10x15 cm) and a distance of at least 3 meters between the source and the breast in

interferometric imaging implies emitting $5x10^{11}$ photons within a 50 mradians cone within 1-2 seconds. A conventional microfocus X-ray tube would take approximately 10 minutes to generate such fluence, clearly unsuitable for clinical applications.

- Laser sources exhibit a broad, synchrotron-like spectrum that matches the wide spectral acceptance of high angular sensitivity interferometers.
- The micrometer-scale spot size offered by laser-based X-ray sources significantly enhances spatial resolution in medical imaging, effectively reaching the limit of detector pixel size. Significantly, the spot size of a laser-generated X-ray source does not increase with higher driving power, as seen with conventional X-ray tubes.
- Another significant advantage of the µm spot source size is the potential elimination of the source grating G_0 in Talbot interferometry. Removing G_0 doubles the available photons for imaging and can also enhance fringe visibility, mainly when the projected source size is small compared to the G_1 period p_1 (equation 2.5 from Chapter 2).
- A micrometer-scale X-ray source enables 2D Talbot interferometry. While current Talbot interferometers mainly use 1D gratings to measure X-ray refraction in a single direction, the use of "checkerboard" gratings in 2D Talbot interferometry has shown significant improvements in the quality and information content of phase images [58].
- An ultrashort X-ray pulse can completely eliminate image blurring caused by organ or patient movement. This characteristic has been proposed for laser-based propagation phase contrast CT in cardiological imaging for small animal models [59].

To evaluate the potential in the medical application of the refraction-enhanced technique with high sensibility and visibility interferometers in conjunction with laser-based microfocus X-ray sources, computations and simulations with XWFP code were performed.

First, the results of simulations using the refraction-enhanced technique for three nylon fibers (1120 µm, 750 µm, and 400 µm) embedded in adipose tissue, similar to the ones from the accredited phantom used in the experiments depicted in Chapter 3, are shown in Figure 4.1. The simulations were conducted using a laser-like X-ray source with a spot size of 2 µm, operating at approximately 33 keV. The detector used had a pixel size of 150 µm and a quantum efficiency of 75%. In this setup, the fringe visibility was assumed at 25%, the magnification M~2, and gratings with a period of 2.4 µm were involved. The total length of the interferometer was 6 meters.

Additionally, in Figure 4.1 b), simulated absorption images obtained using a setup similar to conventional mammography for comparison purposes were included. The X-ray spectrum corresponding to a wolfram tube operated at 28 kVp and filtered with 50 µm of Rhodium foil with a mean energy of 19 keV (representing the energy typically employed in conventional mammography) was used. The distance from the source to the detector was 65 cm, and the detector was placed in close proximity to the object. The magnification for this setup was M~1.

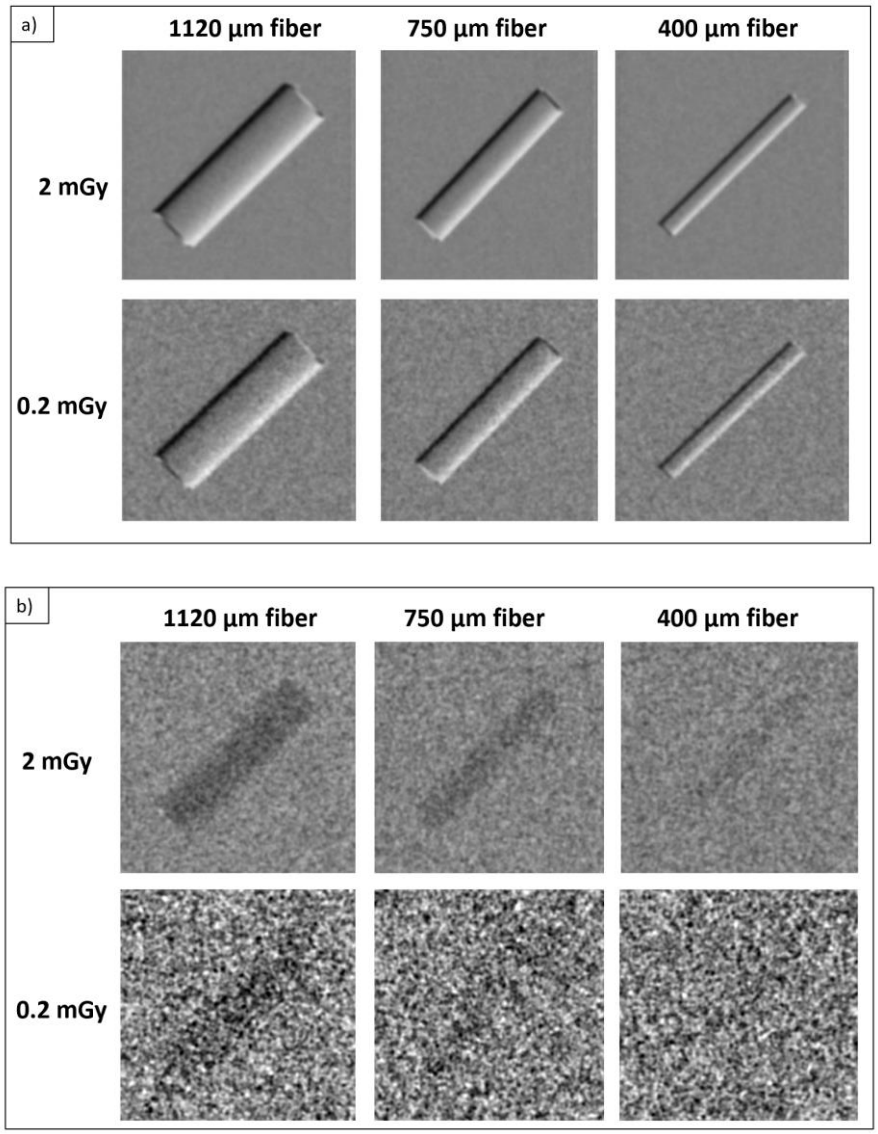

Figure 4. 1. XWFP simulations of nylon fibers of 1120 µm, 750 µm, and 400 µm embedded in adipose tissue at a dose of 2 mGy and 0.2 mGy. a) refraction-enhanced setup. b) mammography-like setup.

These XWFP simulation results validate the benefits of the proposed technique and reveal significantly enhanced visibility of tumor-like objects. These findings indicate the potential for maintaining a high contrast-to-noise ratio (CNR) in the images while reducing the dose to an average value of 0.2 mGy. In contrast, the attenuation images obtained from the mammography-like setup demonstrate that the fibers are barely discernible at a dose of 0.2 mGy, with only a trace indication of the larger fiber (1120 µm). In contrast, the phase images exhibit clear visibility of all the fibers, characterized by well-defined edges and intricate details.

Based on the calculation, simulation and results showcased in the last two Chapters, the combination of high angular sensitivity grating interferometry and laser-driven X-ray sources

shows promise as a new or additional medical imaging technique. For breast interferometric imaging, specific characteristics are needed from laser-driven X-ray sources:

- The mean spectrum energy should fall within the range of approximately 25-40 keV, with a spectral bandwidth of up to $\Delta\lambda/\lambda \sim 1$.
- The photon output per shot should range from several billion to several hundred billion photons emitted within a cone of 50-60 milliradians.
- Ideally, the X-ray spot size should be small enough (<2-3 μm) to generate high fringe visibility without needing a source grating.
- Assuming 5-10 shots for phase stepping, a few hertz or higher pulse rates would be suitable for mammography. Alternatively, if the source is sufficiently bright, a single-shot Moiré fringe imaging approach can be employed.
- In G_0-less Talbot interferometry, maintaining the source position is the most challenging requirement for shot-to-shot stability. However, it may be possible to leverage the variation in source position instead of phase-stepping.

In conclusion, while the requirements for laser-driven X-ray sources are demanding, they are not excessively extreme. This is primarily due to the significant enhancement in soft tissue visibility achieved through high-sensitivity interferometric imaging.

4.2. Perspectives and practical considerations for laser-based medical interferometric imaging

In medical imaging applications, lasers should be typically limited to the 100 TW class (for example, a few joules in 25-30 femtoseconds). This limitation is a result of the significantly higher cost per X-ray photon associated with more powerful lasers. Currently, the cost per photon with higher-power lasers is about a hundred times greater than that of conventional X-ray tubes. This high cost per photon is also the reason why high-power lasers are best suited for high-value imaging applications.

There are two primary mechanisms used to create "all-optical" X-ray sources using lasers: the betatron mechanism and the inverse Compton scattering (ICS) mechanism (as described in references [60, 61, 62, 63, 64, 65]). Both mechanisms rely on Laser Wakefield Acceleration (LWFA) in a gas target to generate micro-sized bunches of ultra-relativistic electrons. These electrons are then oscillated transversely to produce directional synchrotron-like radiation. X-ray sources generated by lasers do not provide a higher output per solid angle as compared to conventional electron-impact X-ray tubes despite being significantly more expensive.

LWFA-accelerated electron bunches typically have charges ranging from tens to hundreds of pico coulombs (pC). The width of the emission cone is approximately on the order of $1/\gamma$, where γ represents the relativistic Lorentz factor of the accelerated electrons. In betatron sources, the electrons undergo a simultaneous acceleration process to several hundreds of MeV and oscillation due to internal plasma fields. In ICS sources, the electrons are accelerated to only several tens of MeV by a first laser pulse. These accelerated electrons collide in a counter-propagating configuration with a second laser pulse of comparable energy. The electric field of the collision laser causes oscillations in the electrons, resulting in the production of X-ray photons with an energy of approximately four times the product of the collision laser photon energy and the square of the relativistic Lorentz factor (γ) of the electrons. The acceleration and collision pulses are typically generated from the same laser system, either through beam division using a pick-off mirror or by reflecting the transmitted portion of the acceleration pulse back using a plasma mirror.

In conclusion, based on simulation and literature, a 100 TW-class laser with a repetition rate of 5-10 Hz would be suitable for PXI of the breast, regardless of whether the betatron or ICS mechanism is used to generate the X-ray source. Lasers with these characteristics are already commercially available. The ICS mechanism may offer the advantage of producing a real point source for G0-less Talbot interferometry.

Furthermore, Figure 4.2 shows a sketch of the ultrahigh sensitivity and low-dose interferometric breast radiography system with an X-ray source generated by lasers. A similar setup has been implemented at the ELETTRA synchrotron for propagation phase contrast imaging of the breast [66]. However, active interferometer stabilization will likely be necessary in a clinical setting to counteract mechanical and thermal disturbances. These stabilization measures are essential to ensure the accuracy and reliability of the imaging process.

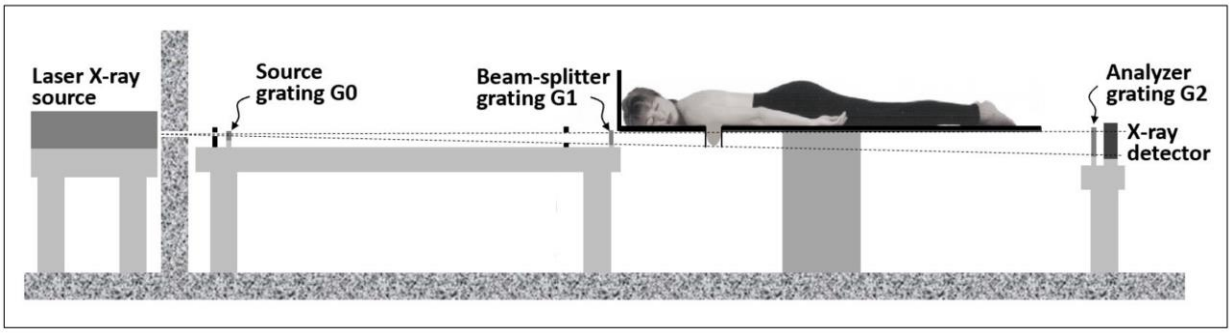

Figure 4. 2. Concept of high sensitivity and low dose interferometric breast imaging system with X-ray source generated by lasers.

In conclusion, addressing practical challenges such as gas target outflow, beam dump shielding, and reducing laser power requirements are crucial steps toward successfully implementing interferometric imaging with laser X-ray sources in clinical settings.

This Chapter suggests that combining ultrahigh sensitive long interferometers with bright, focused, and spatially coherent laser-driven X-ray sources could bring significant benefits on both sides. First, it would enable optimal performance in clinical interferometry, while on the other hand, it would open up a highly impactful application for high-power lasers. Results and simulation show that utilizing expensive laser X-ray sources in conjunction with only propagation phase contrast would not offer significant enough improvements over conventional imaging to make their use attractive in clinics and hospitals.

A part of this work was published in Stutman, D., Safca, N., Tomassini, P., Anghel, E., & Ur, C. A. (2023, June). Towards high-sensitivity and low-dose medical imaging with laser x-ray sources. In Compact Radiation Sources from EUV to Gamma-rays: Development and Applications (Vol. 12582, pp. 35-46). SPIE.

Future Perspectives at ELI-NP

The findings highlighted in this thesis suggest that employing multi-meter long small-period grating interferometers alongside bright and directional laser microfocus X-ray sources could significantly improve imaging sensitivity for soft tissue tumors, lesions, and microcalcifications. These improvements can be achieved at X-ray energies suitable for clinical applications while maintaining low radiation exposure. So, the following goals in this direction are to assess the medical application potential of multi-meter long ultrahigh sensitivity grating interferometers when used in conjunction with bright and directional laser-based microfocus X-ray sources. The work in future five years will primarily focus on two potential applications: high sensitivity and low dose mammography, as well as increased sensitivity and low dose imaging of vascular plaque and microcalcifications. Similar to breast tumors, soft plaque and microcalcifications are also low-contrast and are considered a challenge in medical imaging diagnostics. Following success in this stage, a pre-clinical prototype PXI system will be developed utilizing the ultrahigh sensitivity interferometer concept for each proposed application.

All the optimizations and developments will be performed at the XIL laboratory from ELI-NP. The X-ray Imaging Laboratory (XIL) has been implemented and developed at the ELI-NP facility, specifically focusing on advancing methods and instrumentation for diagnosing the effects of high-power lasers on matter. Further on, one of the primary purposes of this laboratory is to explore the applications of PXI using high-power lasers in medicine for applications such as mammography or cardio-pulmonary applications. The research includes investigating innovative ultrahigh-sensitivity X-ray grating interferometry techniques using laser-based X-ray sources that offer directionality, brightness, and spatial coherence, which are essential for reaching the maximum potential of these methods. This laboratory is equipped with almost all the necessary equipment for these experiments, including X-ray tubes, X-ray optics, different sets of gratings, positioning stages, dosimeters, and detectors.

Further, the X-ray sources generated by lasers will be characterized. The metrology of a source of this kind is complex and may be challenging. It has a significant role in its development and optimization. As described in Subchapter 4.2, this kind of source should meet some fundamental criteria to be suitable for clinical implementation and help achieve the maximum potential of phPXI. For the purpose of a source generated by lasers for medical imaging applications purposes, four parameters should be measured: spectrum, fluence, divergence, and source size.

Conclusions

This thesis focuses on the mammography issue and aims to explore and develop an additional method that can improve the early detection of breast cancer with enhanced sensitivity and low doses. Mammary cancer is the second most prevalent cause of mortality among the female population under 50, following lung cancer, and it remains a significant cause of death beyond this age group. Timely identification of mammary tumors is crucial in reducing mortality rates. Mammography, which employs low-energy X-rays to measure the absorption in soft tissues, is currently considered the best technique for large-scale breast cancer screening in women. Current mammography based on X-ray absorption still has two shortcomings: insufficient sensitivity and specificity to early-stage cancers due to poor differentiation between tumor and normal tissues and relatively large radiation dose.

In this work, a new additional technique for breast cancer detection with higher sensitivity and lower doses is proposed and developed - X-ray phase-contrast or refraction-based imaging with ultrahigh angular sensitivity grating interferometers, having several meters in length. Since conventional X-ray tubes do not emit sufficient photons for clinical imaging at such distances, it was proposed to combine ultrahigh sensitivity grating interferometry with a bright and directional X-ray source driven by a high-intensity femtosecond laser, towards a new imaging modality, laser-based interferometric mammography.

Four main experiments were conducted and presented in this thesis, and the results for each one demonstrate the high potential of the proposed method for interferometric breast radiography and cardio-pulmonary application.

In the first experiment conducted in the XIL laboratory, a 5.7 meters Talbot-Lau Interferometer was developed, in normal incidence configuration, with 2.4 µm period gratings, better than 1 µrad angular sensitivity, and 15% fringe visibility. The study addressed two significant limitations of conventional mammography. The first one is the poor image contrast between normal and tumor tissue due to the minimal differences in X-ray absorption between normal and tumor tissues, and the second one is the radiation dose which is still high. We obtained highly sensitive images of tumor-like objects using an accreditation phantom, revealing intricate details that are often invisible or difficult to identify using conventional mammography. Importantly, we achieved this improved sensitivity at a significantly reduced dose of 0.32 mGy. All images were obtained using different specific acquisition and analysis techniques for phase contrast imaging like phase-stepping procedure, Moiré, and refraction enhanced method at doses ranging between 2.73 mGy and 0.32 mGy. Even though all techniques provided good results with

meaningful information, the best images for this configuration were obtained through the phase-stepping procedure.

Moreover, tests on a real breast tumor sample were done. It should be noted that the samples used in our study were dry and embedded in paraffin and may not accurately represent the natural structure of a tumor within an actual breast. However, despite this limitation, promising results in the darkfield contrast channel were achieved. The tumor is entirely invisible in the absorption image, only revealing the plastic holder of the paraffin. However, in the darkfield image, the entire tumor region becomes visible and can be readily identified, exhibiting some branching patterns within the adipose tissue. In the phase image, the dryness of the tissue and surface irregularities of the paraffin nearly eliminates the signal, although some indications of possible tumor identification can still be observed. To validate the findings, a comparison with microscopic histopathological images of the same samples was performed. The analysis confirmed the results obtained through the phase-contrast imaging technique, even with these specific sample characteristics. The obtained images employing the phase-stepping method and the histopathological images suggest that for fresh tissue samples, the accuracy of the results could be even more precise, with inaccessible critical information about the structure of the tumor.

To have the capability to evaluate and optimize the average radiation dose used in phase contrast medical imaging experiments in the XIL laboratory, it was necessary to develop a dedicated dosimetry methodology. Given the fact that phase contrast imaging based on grating interferometry has not been used at the clinical level so far, there are no protocols for measuring and calculating the radiation dose received by the patient. To have a clear picture for optimizing the performance of the interferometric systems built and the dose reduction under current clinical levels, it was necessary to create a dosimetry system that considers all the elements of the proposed system (geometry, gratings, spectrum, filters). The first part of the dosimetric methodology consists of measuring KERMA in air, and the second consists of calculations and Monte Carlo simulations to obtain the conversion factor necessary for the mean glandular dose absorbed by the breast. A standardized numerical breast phantom with a thickness of 5 cm was utilized to perform the calculations. This phantom consisted of a central region composed of 50% glandular and 50% adipose tissue, covered by a 5 mm thick layer of 100% adipose tissue designed to represent the skin. The tissue compositions recommended by the International Commission on Radiation Units and Measurements (ICRU) in Report 44 were utilized in the calculations. The resulting conversion factor was determined to be 0.464 for our specific experimental configuration. This conversion factor facilitates the calculation of the mean glandular dose by multiplying the measured incident air KERMA by this factor.

The second experiment presented in this work was an extension of the previously presented 5.7 meters long Talbot-Lau with the purpose of improving the fringe visibility while maintaining the same high angular sensitivity by exploring two new improvements to the interferometer performance towards medical applications such as lower dose and increased sensitivity for abnormal structure identification in the breast. A 5.84 meters glancing angle interferometer (GAI)

operating at 45° incidence was built and optimized. Notably, it achieves a remarkable angular sensitivity of 0.82 μradians and a fringe contrast of 22%. The interferometer was utilized to capture images of the same structures that mimic malignant formations at a mean energy of 30 keV. The obtained results provide valuable information and intricate details of these objects, aiding early diagnosis while maintaining a low radiation dose. The phase-stepping method necessitates only 1.68 mGy, whereas the refraction-enhanced technique reduces it to 0.1 mGy. By employing phase-contrast imaging interferometry, this research explored the potential of incorporating it as an additional technique for breast radiography.

Moreover, it showcases the capabilities of the proposed ultrahigh sensitivity GAI interferometer, both with the phase-stepping method and the refraction-enhanced approach, by reducing radiation dosage and enhancing the visibility of tumor-like objects. Even though the results were impressive, there are still unsolved problems. The images obtained through the refraction-enhanced technique using the GAI system exhibit some "moving shadows," which arise from residual Moiré fringes in the GAI system. While successfully Moiré-free images were obtained under normal incidence conditions, aligning and removing Moiré fringes become more challenging when dealing with very long and highly sensitive GAI interferometers. It is crucial to address this issue since the shadows can potentially interfere with the diagnostic process. However, despite this limitation, it is noteworthy that even at a low dose of 0.1 mGy, the fibers mimicking tumors remain visible in both experimental setups. Efforts should be directed toward finding a solution to eliminate these shadows and further enhance the diagnostic quality.

The third experiment explores the possibility of using phase contrast imaging for cardio-pulmonary applications, and it was conducted at the Department of Physics and Astronomy at Johns Hopkins University. Images of a human artery utilizing a long Talbot-Lau Interferometer were obtained, and they show significantly important details in plaque identification. The darkfield image provides valuable supplementary information that goes beyond what is observed in the attenuation and phase images. Within this scatter image, structures within the fatty mass and on the artery wall become visible, in addition to the macrocalcification identified in the attenuation and phase image. These small structures are believed to be cholesterol crystals, which serve as early indicators of thrombosis and atherosclerosis.

Further, on this topic, images of a rat heart were obtained in the XIL laboratory with an ultrahigh sensibility interferometer having 0.87 μradians angular sensitivity. The experiment was conducted with the sample immersed in formalin and the sample in air. The differences in these two cases indicated the importance of the characteristics of the environment. In the situation of the sample immersed in formalin, the phase image provided excellent results with high visibility for the coronary artery, while the dark-field image offered the most impressive results for the sample in the air. In this case, the coronary artery and the space between the heart wall and the pericardial are visible. The results obtained in these two experiments demonstrate the remarkable capabilities of the proposed method for potential cardio-pulmonary applications. However, they also highlight

the necessity to enhance the performance of the technique further and customize it based on specific application requirements.

Moreover, while the presented work in this thesis demonstrates that the proposed technique can be implemented with an X-ray tube, there is potential for substantial improvement in the method to achieve the maximum capabilities of PXI in medical applications. Conventional X-ray sources have limitations with regard to exposure time, sensitivity, spatial resolution, and fringe visibility when it comes to ultra-high sensitivity interferometry. They emit radiation in all directions, and the photon fluence is insufficient for rapid clinical imaging at these extended distances. To achieve optimal results, an ideal source for interferometric mammography should emit a photon fluence of approximately 10^{10} photons/ mm^2 or higher, covering the compressed breast area at distances of several meters. Additionally, the source spot size should ideally be in the range of 1µm, providing spatial coherence. This would significantly enhance spatial resolution, amplify phase effects, and potentially eliminate the need for the source grating.

X-ray sources generated by high-power lasers can be an ideal solution for such medical applications. They offer significantly higher brightness and directionality as compared to conventional tubes, delivering a large number of photons over long distances, within a narrow cone, and in extremely short durations.

The last part of the work presented in this thesis highlighted the possibility of integrating ultrahigh-sensitive long interferometers with intense, well-focused, and spatially coherent X-ray sources generated by high-power lasers. Simulation performed with XWFP with laser-like sources and long Talbot-Lau interferometers on numerical medical phantoms like breast tumors-like objects or blood vessels showed the capability of this method of improving the visibility and decreasing the dose for the patient. This study focused on developing and optimizing the interferometer to be suitable for clinical implementation to achieve increased visibility of the abnormalities or malignancies in tissue and low doses. As concerning laser-based X-ray sources, their development is advancing rapidly, and they could fulfill all the needed requirements for medical interferometric imaging. Betatron X-ray sources are nearing the necessary level of performance for interferometric breast imaging, and initial computational optimization of inverse Compton scattering (ICS) source also shows the promising output for breast imaging, incorporating multiple phase steps. Consequently, by conducting additional theoretical and experimental optimization, it is highly probable to obtain X-ray sources appropriate for medical imaging using 100 TW-class lasers or even in the 10 TW-class.

In conclusion, the experimental data, calculations, and simulations presented in this thesis indicate that phase contrast imaging can become an alternative or additional technique to the conventional medical radiology methods used for screening in the present. Images with increased visibility and low doses of extremely fine details generally associated with early-stage breast cancers or arterial plaque were obtained with the proposed methods. Even though the results

obtained until now are impressive, the maximum capacity of this technique will be accomplished with a coherent, intense, high flux laser-based X-ray source.

However, on the way toward clinical implementation, there are still some difficulties to be solved, beginning with the stability of such a system, exposure time, and the development and optimization of a bright, coherent, capable of high photon fluxes at long distances X-ray source.

Bibliography

1. Jens Als-Nielsen, Des McMorrow. Elements of Modern X-ray Physics - 2nd edition. s.l. : John Wiley & Sons, Ltd, 2011.

2. A.G. Michette, C.J. Buckley. X-ray Science and Technology. s.l. : IOP Publishing Ltd, 1993.

3. Knoll, Glenn F. Radiation Detection and Measurment -3rd edition . s.l. : John Wiley & Sons, Inc., 2000.

4. X-Ray Interactions: Photoabsorption, Scattering, Transmission and Reflection E = 50-30,000 eV, Z = 1-92. B.L. Henke, E.M. Gullikson, and J.C. Davis. 1993, Atomic Data and Nuclear Data Tables, Vol. 54, pp. 181-342.

5. X-ray phase imaging reaching clinical uses. Momose, Atsushi. 2020, Physica Medica, Vol. 79, pp. 93-102.

6. X-ray phase-contrast imaging: from pre-clinical applications towards clinics. Bravin, A., Coan, P., & Suortti, P. 2012, Physics in Medicine & Biology, Vol. 58.

7. Advanced X-ray Imaging Technology. Pfeiffer D, Pfeiffer F, Rummeny E. 2020, Recent Results Cancer Res, Vol. 216, pp. 3-30.

8. X-Ray Phase-Contrast Technology in Breast Imaging: Principles, Options, and Clinical Application. Seyedamir Tavakoli Taba, Timur E. Gureyev, Maram Alakhras, Sarah Lewis, Darren Lockie, and Patrick C. Brennan. 2018, American Journal of Roentgenology, Vol. 211.

9. The application of synchrotron radiation to X-ray interferometry. Hart, M. 1980, Nuclear Instruments and Methods, Vol. 172, pp. 209-214.

10. Subnanoradian X-ray phase-contrast imaging using a far-field interferometer of nanometric phase gratings. Wen, H., Gomella, A., Patel, A. et al. 2013, Nature Communication.

11. Phase objects in synchrotron radiation hard x-ray imaging. Cloetens, P., Barrett, R., Baruchel, J., Guigay, J.-P. and Schlenker, M. 1996, J. Appl. Phys, Vol. 29, pp. 133-146.

12. X-ray Phase Contrast Imaging from Synchrotron to Conventional Sources: A Review of the Existing Techniques for Biological Applications. Laurene Quenot, Sylvain Bohic and Emmanuel Brun. 2022, Appl. Sci., Vol. 12.

13. Performance evaluation of x-ray differential phase contrast computed tomography (P.C.T.) with respect to medical imaging. Rainer Raupach, Thomas Flohr. 2012, Medical Physics, Vol. 39, pp. 4761-4774.

14. Analytical evaluation of the signal and noise propagation in x-ray differential phase-contrast computed tomography. Raupach R, Flohr TG. 2011, Phys Med Biol. , Vol. 56, pp. 2219-44.

15. Edge-illumination x-ray phase-contrast imaging. Olivo, Alessandro. 2021, Journal of Physics: Condensed Matter, Vol. 33.

16. Talbot phase-contrast x-ray imaging for the small joints of the hand. Stutman D, Beck TJ, Carrino JA, Bingham CO. 2011, Phys Med Biol, Vol. 56, pp. :5697-720.

17. , X-ray phase imaging with a grating interferometer. [12] Timm Weitkamp, Ana Diaz, Christian David, Franz Pfeiffer, Marco Stampanoni, Peter Cloetens, and Eric Ziegler. 2005, Opt. Express, Vol. 13, pp. 6296-6304.

18. Phase retrieval and differential phase-contrast imaging with low-brilliance X-ray sources. F. Pfeiffer, T. Weitkamp, O. Bunk, C. David. 2006, Nature Phys, Vol. 2, pp. 258-261.

19. High sensitivity X-ray phase contrast imaging by laboratory grating-based interferometry . Joan Vila-Comamala, Lucia Romano, Konstantins Jefimovs, Hector Dejea, Anne Bonnin, Andrew C. Cook, Ivo Planinc, Maja Cikes, Zhentian Wang, and Marco Stampanoni. 2021, Opt. Express, Vol. 29, pp. 2049-2064.

20. X-ray dark-field chest imaging: qualitative and quantitative results in healthy humans. Gassert, Florian T., Theresa Urban, Manuela Frank, Konstantin Willer, Wolfgang Noichl, Philipp Buchberger, Rafael Schick et al. 2021, Radiology, Vol. 301, pp. 385-395.

21. X-ray dark-field chest imaging for detection and quantification of emphysema in patients with chronic obstructive pulmonary disease: a diagnostic accuracy study. Willer, Konstantin, Alexander A. Fingerle, Wolfgang Noichl, Fabio De Marco, Manuela Frank, Theresa Urban, Rafael Schick et al. 2021, The Lancet Digital Health, Vol. 3, pp. 733-744.

22. Dark-field computed tomography reaches the human scale. Viermetz, Manuel, Nikolai Gustschin, Clemens Schmid, Jakob Haeusele, Maximilian von Teuffenbach, Pascal Meyer, Frank Bergner et al. 2022, Proceedings of the National Academy of Sciences , Vol. 119.

23. World Health Organization. [Online] [Cited: iunie 30, 2023.] https://www.who.int/news-room/fact-sheets/detail/breast-cancer.

24. American Cancer Society. [Online] [Cited: iunie 30, 2023.] https://www.cancer.org/cancer/types/breast-cancer/screening-tests-and-early-detection/mammograms/limitations-of-mammograms.html.

25. . Non-invasive classification of microcalcifications with phase-contrast X-ray mammography. [3] Wang, Z., Hauser, N., Singer, G. et al. 2014, Nat Commun, Vol. 5.

26. Recent advances in X-ray imaging of breast tissue: From two- to three-dimensional imaging. L. Heck, J. Herzen. 2020, Physica Medica, Vol. 79, pp. 69-79.

27. Behling, Rolf. MODERN DIAGNOSTIC X-RAY SOURCES. s.l. : Taylor & Francis Group, LLC, 2016.

28. Synchrotron radiation and structural proteomics. al., Pechkova et. 2011, CRC Press.

29. Optimization of propagation-based x-ray phase-contrast tomography for breast cancer imaging. Baran, Patrycja, et al. 6, 2017, Physics in Medicine & Biology, Vol. 62, p. 2315.

30. X-ray phase-contrast imaging. Endrizzi, M. 2018, Nuclear instruments and methods in physics research section A: Accelerators, spectrometers, detectors and associated equipment, Vol. 878, pp. 88-98.

31. On the evolution and relative merits of hard X-ray phase-contrast imaging methods. al., Wilkins S. et. 2010, Phil. Trans. R. Soc. A, Vol. 372, p. 20130021.

32. X-ray phase contrast imaging: From synchrotrons to conventional sources. Olivo A., Castelli E. 2014, La rivista del nuovo cimento , Vol. 37, pp. 467-508.

33. "Medical phase contrast x-ray imaging: current status and future prospects. Lewis, Robert A. 16, 2004, Physics in medicine & biology, Vol. 49, p. 3573.

34. Development of phase-contrast X-ray imaging techniques and potential medical applications. Zhou, Shu-Ang, and Anders Brahme. 3, 2008, Physica Medica, Vol. 24, pp. 129-148.

35. Tailless X-Ray Single-Crystal Reflection Curves Obtained By Multiple Reflection. Bonse, U., and M. Hart. 9, 1965, Applied Physics Letters, Vol. 7, pp. 238-240.

36. The application of synchrotron radiation to X-ray interferometry. Hart, Michael. 1-2, 1980, Nuclear Instruments and Methods, Vol. 172, pp. 209-214.

37. Coherent X-ray Optics. Paganin, D. M. 2006, Oxford University Press.

38. Holotomography: Quantitative phase tomography with micrometer resolution using hard synchrotron radiation x rays. P. Cloetens, et al. 19, 1999, Appl. Phys. Lett, Vol. 75.

39. Phase-contrast imaging using polychromatic hard X-rays. Wilkins, S. W., et al. 6607, 1996, Nature, Vol. 384, pp. 335-338.

40. X-ray phase contrast imaging of biological specimens with femtosecond pulses of betatron radiation from a compact laser plasma wakefield accelerator. Kneip, S., et al. 9, 2011, Applied Physics Letters, Vol. 99.

41. Facts relating to optical science. Talbot, H. F. 4, 1836, The London, Edinburgh, and Dublin Philosophical Magazine and Journal of Science, pp. 401-407.

42. Wild, R. The Talbot effect. 2005 .

43. Phase-contrast radiographs of nonstained rat cerebellar specimen. Momose, Atsushi, and Jun Fukuda. 4, 1995, Medical physics , Vol. 22, pp. 375-379.

44. X-ray dark-field and phase-contrast imaging using a grating interferometer. Pfeiffer, F., et al. 20, 2009, Journal of Applied Physics 105.10 , Vol. 105.

45. Slit-scanning differential x-ray phase-contrast mammography: Proof-of-concept experimental studies. al., Koehler et. 2015, Medical physics, Vol. 42.

46. Demonstration of X-ray Talbot interferometry. Momose, Atsushi, et al. 7B, 2003, Japanese journal of applied physics, Vol. 42, p. L866.

47. A universal moiré effect and application in X-ray phase-contrast imaging. Miao, Houxun, et al. 9, 2016, Nature physics, Vol. 12, pp. 830-834.

48. Berns EA, Pfeiffer DE, Butler PF, et al. ACR - American College of Radiology Digital mammography - Quality Control . s.l. : College of Radiology, 2020.

49. New Capabilities of the FLUKA Multi-Purpose Code. al., C. Ahdida et. 2022, Frontiers in Physics , Vol. 9.

50. FLAIR: A Powerful But User Friendly Graphical Interface For FLUKA. Vlachoudis, V. 2009, Proc. Int. Conf. on Mathematics, Computational Methods & Reactor Physics, Vols. Saratoga Springs, New York.

51. Toward Clinically Compatible Phase-Contrast Mammography. Scherer K, Willer K, Gromann L, Birnbacher L, Braig E, Grandl S, et al. 6, 2016, PLoS ONE, Vol. 10.

52. Dose-compatible grating-based phase-contrast mammography on mastectomy specimens using a compact synchrotron source. Eggl, E., Grandl, S., Sztrókay-Gaul, A. et al. 2018, Sci Rep, Vol. 8.

53. Low-dose, simple, and fast grating-based X-ray phase-contrast imaging. Peiping Zhu, Kai Zhang, Zhili Wang, Yijin Liu, Xiaosong Liu, Ziyu Wu, Samuel A. McDonald, Federica Marone, and Marco Stampanoni. 31, 2010, PNAS, Vol. 107, pp. 13576-13581.

54. "High Energy X-ray Phase-Contrast Imaging Using Glancing Angle Grating Interferometers. Stutman D., Stayman J.W., Finkenthal M., Siewerdsen J.H. 2013, Proc SPIE, Vol. 8668.

55. High energy x-ray phase contrast CT using glancing-angle grating interferometers. Sarapata, A., Stayman, J.W., Finkenthal, M., Siewerdsen, J.H., Pfeiffer, F. and Stutman, D. 2014, Med. Phys., Vol. 41.

56. High aspect ratio gratings for X-ray phase contrast imaging. Jürgen Mohr, Thomas Grund, Danays Kunka, Johannes Kenntner, Juerg Leuthold, and Jan Meiser. 2012, AIP Conference Proceedings, pp. 41-50.

57. Phase-Contrast CT: Qualitative and Quantitative Evaluation of Atherosclerotic Carotid Artery Plaque. Holger Hetterich, Marian Willner, Sandra Fill, Julia Herzen, Fabian Bamberg, Alexander Hipp,Ulrich Schüller, Silvia Adam-Neumair, Stefan Wirth, Maximilian Reiser, Franz Pfeiffer, Tobias Saam. 3, 2014, RSNA Radiology, Vol. 271.

58. X-ray phase contrast imaging and noise evaluation using a single phase grating interferometer. J. Rizzi, P. Mercère, M. Idir, P. Da Silva, G. Vincent, and Jérôme Primot. 2013, Optics Express, Vol. 21, p. 17340.

59. Numerical simulation of novel concept 4D cardiac microtomography for small rodents based on all-optical Thomson scattering X-ray sources. Panetta, D., Labate, L., Billeci, L. et al. 8439, 2019, Sci. Rep., Vol. 9.

60. Thomson backscattering X-rays from ultra-relativistic electron bunches and temporally shaped laser pulses. al., P. Tomassini et. 2005, Appl. Phys., Vol. 80, pp. 419-436.

61. Production of high-quality electron beams in numerical experiments of laser wakefield acceleration with longitudinal wave breaking. al., P. Tomassini et. 121301, 2003, Phys. Rev. Acc. Beams, Vol. 6.

62. Femtosecond x-rays from Thomson scattering using laser wakefield accelerators. P. Catravas, E. Esarey, W.P. Leemans. 1828, 2001, Meas. Sci. Technol, Vol. 12.

63. Particle injection into the wave acceleration phase due to nonlinear wake wave breaking. al., S.V. Bulanov et. R5257, 1998, Phys. Rev., Vol. E 58.

64. Femtosecond x rays from laser-plasma accelerators. S. Corde, K. Ta Phuoc, G. Lambert, et al. 1, 2013, Rev. Mod. Phys, Vol. 85.

65. Laser wakefield accelerator based light sources: potential applications and requirements. F. Albert, A. G. R. Thomas, S. P. D. Mangles, S. Banerjee, S. Corde, A. Flacco, M. Litos, D. Neely, J. Vieira, Z. Najmudin. 084015, 2014, Plasma Phys. Control. Fusion, Vol. 56.